Entrainment and detrainment statistics of a stationary shallow cumulus cloud

Huang, Jingzi; Burridge, Henry C.; de Roode, Stephan R.; van Reeuwijk, Maarten

DOI
10.1002/qj.4920

Publication date
2025

Document Version
Final published version

Published in
Quarterly Journal of the Royal Meteorological Society

Received: 19 September 2024 | Revised: 22 November 2024 | Accepted: 2 December 2024

DOI: 10.1002/qj.4920

Quarterly Journal of the Royal Meteorological Society RMetS

RESEARCH ARTICLE

Entrainment and detrainment statistics of a stationary shallow cumulus cloud

Jingzi Huang[1] | **Henry C. Burridge**[1] | **Stephan R. de Roode**[2] | **Maarten van Reeuwijk**[1]

[1]Department of Civil and Environmental Engineering, Imperial College London, London, UK

[2]Faculty of Civil Engineering and Geosciences, Delft University of Technology, Delft, The Netherlands

Correspondence
Jingzi Huang, Department of Civil and Environmental Engineering, Imperial College London, London SW7 2AZ, UK.
Email: jingzi.huang17@imperial.ac.uk

Funding information
UK Turbulence Consortium (EPSRC grant EP/R029326/1)

Abstract

A fully resolved shallow cumulus cloud simulation (albeit at a lower Reynolds number than in the atmosphere) is performed in a quiescent environment to investigate instantaneous entrainment and detrainment. Despite constant boundary conditions and environment, the cloud displays cyclic puff-like behaviour, indicating that puffs are an intrinsic feature of the system not linked to thermals in the sub-cloud region. The cloud dynamics are examined via both Reynolds-averaged statistics and conditionally averaged statistics. The Reynolds-averaged statistics reveal that the majority of entrainment occurs over the upper part of cloud and that the cloud creates an intrusion at about its half height (about 1,000 m) through which it detrains. Using a novel technique that enables direct evaluation of instantaneous entrainment and detrainment fluxes, we examine instantaneous entrainment and detrainment at two interfaces: (1) the cloud boundary, which separates the cloud from the environment; and (2) the updraught boundary, which separates the rising flow (updraught) from the descending flow (subsiding shell). The data show that the entrainment and detrainment rates are a factor of 2 larger than those estimated from the bulk assumption, consistent with other studies. Furthermore, entrainment is strongly correlated to the rising puffs, as evidenced by conditioning the statistics on the instantaneous buoyancy.

KEYWORDS

bulk microphysics, direct numerical simulation, entrainment and detrainment, large-eddy simulation, shallow cumulus clouds

1 | INTRODUCTION

The consequences of cloud dynamics on the global energy balance provide one of the greatest uncertainties in predictions of weather and climate (Bony *et al.*, 2015; Bretherton, 2015; Stephens & Kummerow, 2007). Despite their relatively small scale, shallow cumulus clouds contribute substantially to this uncertainty in numerical weather prediction models, as cumulus convection is one of the most important unresolved processes in the atmosphere (de Rooy *et al.*, 2013). The mixing of ambient air into a cumulus cloud, by the process termed "entrainment", dilutes the buoyancy of the moist shallow cumulus cloud air and significantly influences its evolution.

Moreover, the dynamics resulting from this entrainment of ambient air can ultimately alter the lifespan of these shallow cumulus clouds by causing them to dissipate; this terminal stage is associated with strong detrainment of air from the cloud back into the atmosphere (Heus *et al.*, 2009; Zhao & Austin, 2005). Moreover, entrainment and detrainment can coexist across the cloud boundary instantaneously. As such, the entrainment and detrainment dynamics of shallow cumulus clouds have received substantial interest (e.g., de Roode *et al.*, 2012; de Rooy *et al.*, 2013; Siebesma *et al.*, 2003).

Entrainment and detrainment are hard to measure in the field or laboratory, since exchange rates tend to be small compared with the characteristic velocity scales. In recent decades, many studies have exploited developments in computing technologies and deployed large-eddy simulations (LESs) to investigate these processes over large-scale "cloud fields" containing a large number of clouds. These simulations can account for relevant observed atmospheric conditions (e.g., the sub-cloud layer); (see de Rooy *et al.*, 2013, for a review). The results have provided useful insights that have been widely incorporated in numerical weather prediction and climate models.

Entrainment and detrainment rates across a cloud boundary at fixed height are typically defined as, respectively (de Rooy *et al.*, 2013; Siebesma, 1998),

$$E_\phi = -\frac{1}{A\phi_\mathrm{e}} \int_{\partial\Omega_\mathrm{E}} \boldsymbol{n}\cdot(\boldsymbol{u}-\boldsymbol{u_i})\phi \; dl, \tag{1}$$

$$D_\phi = -\frac{1}{A\phi_\mathrm{c}} \int_{\partial\Omega_\mathrm{D}} \boldsymbol{n}\cdot(\boldsymbol{u}-\boldsymbol{u_i})\phi \; dl, \tag{2}$$

where $\boldsymbol{u}$ is the fluid velocity, $\boldsymbol{u}_i$ is the interface velocity, and ϕ is the chosen (conserved) scalar of interest. The subscripts "c" and "e" denote characteristic values of the cloud and background environment respectively. The cloud has cross-sectional area A at a fixed height, and $\boldsymbol{n}$ denotes the outward in-plane normal across the horizontally oriented cloud boundary $\partial\Omega = \partial\Omega_\mathrm{E} \cup \Omega_\mathrm{D}$, where $\partial\Omega_\mathrm{E}$ is the entrainment region for which $|\boldsymbol{n}\cdot(\boldsymbol{u}-\boldsymbol{u_i})| < 0$, and $\partial\Omega_\mathrm{D}$ is a detrainment region for which $|\boldsymbol{n}\cdot(\boldsymbol{u}-\boldsymbol{u_i})| > 0$.

However, the aforementioned entrainment and detrainment rates cannot be practically assessed from most LES datasets since there is no means to explicitly calculate the boundary integral required to evaluate Equations 1 and 2 from standard LES data. Instead, for most LESs reported to date, inferences of the entrainment and detrainment are made by evaluating the residual budgets of the conservation equations of ϕ and evoking a "bulk assumption"; that is, the assumption that the properties of the entrained and detrained fluid (e.g., liquid water potential temperature and total water specific humidity) can be appropriately represented by the characteristic (in the case of the cloud often integral-averaged) scales associated with the environment and the cloud respectively (Betts, 1973; de Roode *et al.*, 2012; Siebesma *et al.*, 2003). Assessment of entrainment via the local boundary values using Equations 1 and 2 has been presented by, for example, Romps (2010); Dawe and Austin (2011); however, owing to the very nature of LESs and their intended resolution, the local boundary and boundary properties of the clouds were estimated using a subgrid interpolation. As reviewed in Mellado (2017), the small scale of dynamics at the cloud boundaries are key to determine the cloud entrainment and the high-resolution simulations start to reveal the laws for the cloud entrainment, accounting for key physical processes. Herein, we capitalise on recent work that allows us to independently, and explicitly, calculate the entrainment and detrainment fluxes across interfaces via a fully resolved numerical simulation (Huang *et al.*, 2023a, 2023b; Van Reeuwijk *et al.*, 2021).

Following Van Reeuwijk *et al.* (2021), we distinguish between "global entrainment" and "local entrainment". Global entrainment refers to the entrainment associated with Reynolds-averaged statistics of the flow, which inherently requires an interface (e.g., the one separating the turbulent flow from non-turbulent background) over which to integrate and a time interval over which to apply the Reynolds decomposition to the flow. For many canonical flows, such as jets, plumes, gravity currents, and so forth, consideration of this "global entrainment" has become the default entrainment closure (e.g., Fernando, 1991; Townsend, 1976; Turner, 1986). Attempts to describe entrainment in shallow cumulus clouds using these global closures have been attempted (Morton *et al.*, 1956; Squires & Turner, 1962) but were largely abandoned for two reasons. First, the cloud is transient, and will behave differently in the different stages of its life cycle, implying that a steady-state model is not appropriate (Katzwinkel *et al.*, 2014; Zhao & Austin, 2005). Second, weather and climate models typically operate at a relatively coarse horizontal resolution (e.g., 10–100 km) in which a single grid cell might capture an ensemble of cumulus clouds, so that it is more pragmatic to model an ensemble cloud field that can be incorporated into climate and weather prediction models (Arakawa & Schubert, 1974). Local entrainment refers to an examination of the pointwise transfer of mass, momentum, and buoyancy across, and integrated along, an instantaneous interface separating the turbulent region from either a non-turbulent or differently turbulent region (Corrsin, 1956; Da Silva *et al.*, 2014). The interface can be convoluted and typically has multiscale fractal properties (Everson & Sreenivasan, 1992). The methods associated with Equations 1 and 2 are local.

Relevant existing work that used the framework outlined in Van Reeuwijk *et al.* (2021) has focused on single-phase flows. Huang *et al.* (2023a) applied the global entrainment framework to a turbulent fountain—a negatively buoyant fluid ejected upwards into a neutrally buoyant environment such that the ejected fluid rises, decelerates, and eventually falls back. The relevant aspect of the fountain is that, like shallow cumulus clouds, rising and falling flows coexist, implying that there are several interfaces one can consider. For the turbulent fountain one can consider a turbulent–non-turbulent interface that separates the ambient environmental fluid from the turbulent fountain, but also an internal turbulent–turbulent interface that separates the rising upflow from the falling downflow. For shallow cumulus clouds, the interface distinguishing the cloud from the environment is a turbulent–non-turbulent interface and the interface distinguishing updraught and subsiding shell is a turbulent–turbulent interface (Abma *et al.*, 2013; Heus & Jonker, 2008; Nair *et al.*, 2021). Huang *et al.* (2023b) examined the turbulent fountain flows using the local entrainment framework of Van Reeuwijk *et al.* (2021) combined with the computational methods described in Yurtoglu *et al.* (2018), enabling explicit calculation of instantaneous entrainment and detrainment fluxes across both conditionally sampled turbulent–non-turbulent and turbulent–turbulent interfaces. This local framework provided an underlying perspective on the entrainment to complement insights from the study of the global entrainment.

The aim of this article is to apply the methodologies of Huang *et al.* (2023b) to shallow cumulus clouds to provide independent measurements of the segregated entrainment and detrainment fluxes that coexist in shallow cumulus clouds. In order to do so, we construct an idealised set-up of a single cumulus cloud in a quiescent environment. The simulation comprises the atmosphere from the cloud base upwards, and moist warm fluid is steadily ejected from a circular source at the cloud base. The ambient environment is maintained close to its original state (by way of a nudging scheme; see Section 2 for details) to avoid cloud conditioning of the atmosphere, thus aiming to produce a steady-state cumulus cloud, perhaps reminiscent of the cumulus clouds that can form as moist air travels up a mountain causing a stationary cloud (Elvidge & Renfrew, 2016; Whiteman, 2000).

Fully resolved flow and scalar fields are necessary for the estimation of the instantaneous entrainment fluxes using the method outlined in Huang *et al.* (2023b). Therefore, direct numerical simulation was carried out in a full cloud height scale and was solved using the Navier–Stokes equations without using any turbulence closure models. To be able to simulate the full-height cumulus cloud whilst keeping the simulation computationally tractable, the kinematic viscosity and diffusivities were modified from their physical values to ensure an appropriate number of length scales remain resolved by the computational grid. As such, the set-up resembles a numerical cloud chamber, since all of the relevant cloud physics is represented but the number of active scales is fewer than in the full atmosphere. The article is organised as follows: in Section 2 we describe the numerical simulation details and initial profiles. In Section 3 we describe the instantaneous and time-averaged cumulus cloud observation and discuss the internal cloud structure. In Section 4 we introduce and examine the integral quantities including the net entrainment from both global and local perspectives, and from the local perspective we investigate the segregated entrainment and detrainment events of the cloud, linking them to the cloud dynamics. Conclusion remarks are made in Section 5.

2 | SIMULATION DETAILS

The governing equations for the fluid motion are (e.g., Wyngaard, 2010)

$$\nabla \cdot \boldsymbol{u} = 0, \tag{3}$$

$$\frac{\partial \boldsymbol{u}}{\partial t} + \nabla \cdot \boldsymbol{u}\boldsymbol{u} + \nabla p = \nu \nabla^2 \boldsymbol{u} + b\boldsymbol{e}_z, \tag{4}$$

where $\boldsymbol{u}$ is the velocity, t is the time, $\boldsymbol{e}_z$ is the unit vector in the z-direction, ν is the (effective) kinematic viscosity of air, and p is the deviatoric local kinematic pressure:

$$p(\boldsymbol{x}, t) \equiv \frac{P(\boldsymbol{x}, t) - p_\mathrm{h}(z)}{\rho_e(z)}, \tag{5}$$

where $\rho_e(z)$ is the density of the stratified background atmospheric environment (defined later). $P(\boldsymbol{x}, t)$ is the local total pressure, and $p_\mathrm{h}(z)$ is the local hydrostatic pressure. The hydrostatic pressure p_h is defined as

$$\frac{dp_\mathrm{h}(z)}{dz} \equiv -\rho_e(z)g, \tag{6}$$

which can be solved using the ideal gas law (Arabas *et al.*, 2023; Wyngaard, 2010). The buoyancy b in Equation (4) is defined as

$$b \equiv g\frac{\theta_\mathrm{v}(\boldsymbol{x}, t) - \theta_{\mathrm{v,e}}(z)}{\theta_{\mathrm{v,e}}(z)}, \tag{7}$$

where $\theta_\mathrm{v}(\boldsymbol{x}, t)$ is the local virtual potential temperature and $\theta_{\mathrm{v,e}}(z)$ is the background environmental virtual potential temperature, which is also a function height, and g is the gravitational acceleration. The virtual potential temperature is defined as (Wyngaard, 2010)

$$\theta_v = \theta\left[1 + \left(\frac{R_v}{R_d} - 1\right)q_t - \frac{R_v}{R_d}q_l\right], \tag{8}$$

where θ is the potential temperature, q_t is the total water specific humidity, q_l is the liquid water specific humidity and is zero for the background environment, $R_d = 287.0\,\mathrm{J}\cdot\mathrm{kg}^{-1}\cdot\mathrm{K}^{-1}$ and $R_v = 461.5\,\mathrm{J}\cdot\mathrm{kg}^{-1}\cdot\mathrm{K}^{-1}$ are the gas constants for dry air and water vapour respectively.

Prognostic equations are solved for the liquid water potential temperature $\theta_l(\boldsymbol{x}, t)$ and the total water specific humidity $q_t(\boldsymbol{x}, t)$, given by

$$\frac{\partial\theta_l}{\partial t} + \nabla\cdot\boldsymbol{u}\theta_l = \kappa\nabla^2\theta_l, \tag{9}$$

$$\frac{\partial q_t}{\partial t} + \nabla\cdot\boldsymbol{u}q_t = D\nabla^2 q_t, \tag{10}$$

where κ is the (effective) molecular diffusivity of liquid water droplets and D is the (effective) molecular diffusivity of water vapour. Note that we neglect the effects of radiation and precipitation as the focus is the shallow cumulus clouds (Siebesma, 1998).

The partitioning between water in the liquid and gas phases is determined using the Sommeria and Deardorff (1977) saturation adjustment model. This model assumes that there is no liquid water if the total specific humidity q_t is lower than the saturation specific humidity q_s. If the total specific humidity exceeds the saturation specific humidity, then condensation occurs and $q_l = q_t - q_s$. Saturation adjustment schemes do not allow for a partial saturation at subgrid scales, which can cause artefacts such as artificial evaporation (Wang *et al.*, 2003). However, errors in the buoyancy associated with spurious evaporative cooling are proportional to the grid size. The resolutions used for the simulation used in this article are very high, and thus we do not expect these to play an important role. Furthermore, saturation adjustment schemes do not allow for supersaturation effects, which means they can overestimate latent heating, because in reality some water vapour is left in the supersaturated state (Grabowski & Morrison, 2021). However, recent observations by Siebert and Shaw (2017) show that supersaturations in shallow cumulus clouds are small, on the order of 1%, and will therefore not have a substantial impact on latent heating.

The implementation of the Sommeria and Deardorff (1977) model has been taken from the open-source LES code DALES (Arabas *et al.*, 2023; Siebesma, 1998), which is an established code for cloud simulation that has been extensively validated with observations from experimental field campaigns (Heus *et al.*, 2010).

The simulation domain (Figure 1) has a width, breadth, and height of $5,000 \times 5,000 \times 4,000\,\mathrm{m}^3$. It has its origin at the bottom centre, where the active cloud is generated by vertically injecting moist air into the domain using a circular source of a general cloud size $r_0 = 250\,\mathrm{m}$. In the vertical direction, the domain starts at the cloud base, implying that no sub-cloud dynamics will be resolved. It is clearly impossible to perform direct numerical simulation at this scale. As stated in Section 1, we perform quasi-direct numerical simulation by using values of viscosity and diffusivity that allow resolving all active length scales on the computational grid (here $2,560^3$). For this grid, the lowest value of the kinematic viscosity possible is $\nu = 0.1\,\mathrm{m}^2\cdot\mathrm{s}$, and $\kappa = D = \nu\,\mathrm{Pr}$, where $\mathrm{Pr} = 0.71$. With these values, the grid size is generally resolved smaller than one Kolmogorov length scale; specifically, the grid size $\Delta x \approx 0.8\eta_K$. Here, the Kolmogorov scale $\eta_K = \nu^{3/4}\epsilon^{-1/4}$, where ϵ is the averaged integral dissipation rate of turbulent kinetic energy over the entire cloud height.

The background environment conditions, imposed within the nudging region of the simulation domain, that enable statistically steady metrics to be obtained are now described. The atmospheric environment profiles and boundary conditions were informed by the Barbados Oceanographic and Meteorological Experiment (BOMEX; Holland & Rasmusson, 1973), the Rain in Shallow Cumulus Clouds (RICO; Rauber *et al.*, 2007) field campaign and the LESs of Siebesma *et al.* (2003). In the Barbados Oceanographic and Meteorological Experiment case, there is a thermal inversion layer at the top of the domain where the atmosphere is absolutely stable to ensure all the clouds are colder than the environment and stop rising. This leads to a piecewise function of background environmental values (e.g., the liquid water potential temperature and the total water specific humidity) comprised of two linear profiles. However, to maximise the insights provided by the case considered herein, we strive to minimise the number of length scales imposed within our choice of set-up. The RICO campaign measurements show that it is not always necessary for the environmental potential temperature to exhibit an inversion to arrest the rising clouds. These measurements show that a portion of the active clouds have already stopped rising due to evaporative cooling before reaching the inversion layer. We therefore restrict ourselves to a single linear profile of liquid water potential temperature (i.e., without an inversion layer) and total water specific humidity in the background environment and hence avoid introducing further length scales within our parametrisation of the environment. Doing so required careful tuning of the source conditions, such as the source momentum flux, the liquid water potential temperature, and the total water specific humidity of the injected fluid, to ensure the cloud stays within the simulation domain. Therefore, our somewhat idealised atmospheric state is constructed from the RICO case,

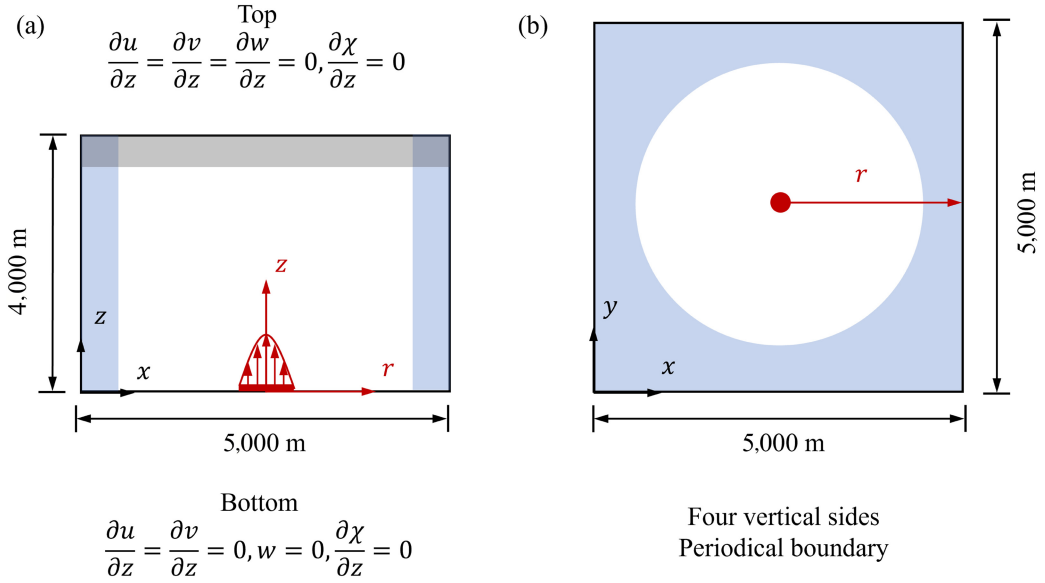

FIGURE 1 Cross-sectional views through the simulation domain: (a) a vertical plane through the centre of the source; (b) a horizontal plane within the domain. The simulation boundary conditions are labelled. At the sides of the domain, the light blue shaded region illustrates the nudging region, in which the nudging terms force the liquid water potential temperature θ_l and total specific humidity q_t towards values appropriate for the background environment. At the top of the domain, the grey shaded region illustrates the region within which the vertical velocity w is nudged towards zero. The location of the source and its parabolic initial velocity are highlighted by the illustration in (a), and the coordinate systems, including the cylindrical coordinate employed within the azimuthal Reynolds average, are marked in both (a) and (b). For a clear visualisation, the width of the source and nudging area are not drawn to scale.

with appropriate adjustment; that is, the linear profiles of the background environmental liquid water potential temperature $\theta_{l,e}$(K) and the background environmental total water specific humidity $q_{t,e}$(kg · kg^{-1}) are given by

$$\theta_{l,e} = 298.81 + \Gamma_{\theta_{l,e}} z, \quad q_{t,e} = 0.0162 - \Gamma_{q_{t,e}} z, \tag{11}$$

where $\Gamma_{\theta_{l,e}} = 4.0 \times 10^{-3}$ K· m^{-1} and $\Gamma_{q_{t,e}} = 4.0 \times 10^{-6}$ kg· kg^{-1} · m^{-1} are the lapse rates of the environmental $\theta_{l,e}$ and $q_{t,e}$ respectively, and z(m) denotes the height from the domain bottom (cloud base). These profiles are shown in Figure 2a,b.

The quasi-steady shallow cumulus cloud is formed by injecting moist fluid vertically upwards from a maintained circular source. The inflow conditions at the source are steady with the values estimated from the RICO cloud base, given as (marked as the dashed lines in Figure 2a,b)

$$\theta_{l,0} = 298.667 \text{ K}, \quad q_{t,0} = 0.0170 \text{ kg} \cdot \text{kg}^{-1}. \tag{12}$$

The inflow boundary condition ensures that at the source the rising flow is non-cloudy (i.e., zero liquid water specific humidity) and neutrally buoyant but will condense and release the latent heat immediately as it rises due to the source momentum, thereby becoming cloudy and positively buoyant and initialising the formation of a shallow cumulus cloud. Figure 2c,d shows the evolution of the injected fluid assuming all processes are adiabatic, as indicated by the dashed lines, showing that the fluid is always positively buoyant (as its virtual potential temperature is greater than that of the background environment) and condenses in the absence of mixing and would lead to ever-accelerating fluid parcels. Naturally, the fluid will mix with the relatively dry environment, which causes evaporation of cloud water, thereby reducing its buoyancy and, with sufficient mixing, becoming negatively buoyant to stop rising.

The radial profile of the vertical velocity of the fluid injected at the source is taken to be parabolic, as a consequence of the sub-cloud layer dynamics, and is taken to follow

$$w_0(r) = w_m \left[1 - \left(\frac{r}{r_0}\right)^2\right], \tag{13}$$

where $w_m = 0.8$ m·s^{-1} is the centre-line velocity, r is the distance from the centre line in the source area, and r_0 is the radius of the source. Knowing that in the atmosphere the fluid from the sub-cloud layer is highly turbulent, turbulence is herein initiated by applying an uncorrelated perturbation of 20% to the velocities in the first cell above the source (Craske & Van Reeuwijk, 2015). These boundary conditions, together with the environment, create a relatively active and high cumulus cloud that covers about half of the domain height and less than 15% of the domain

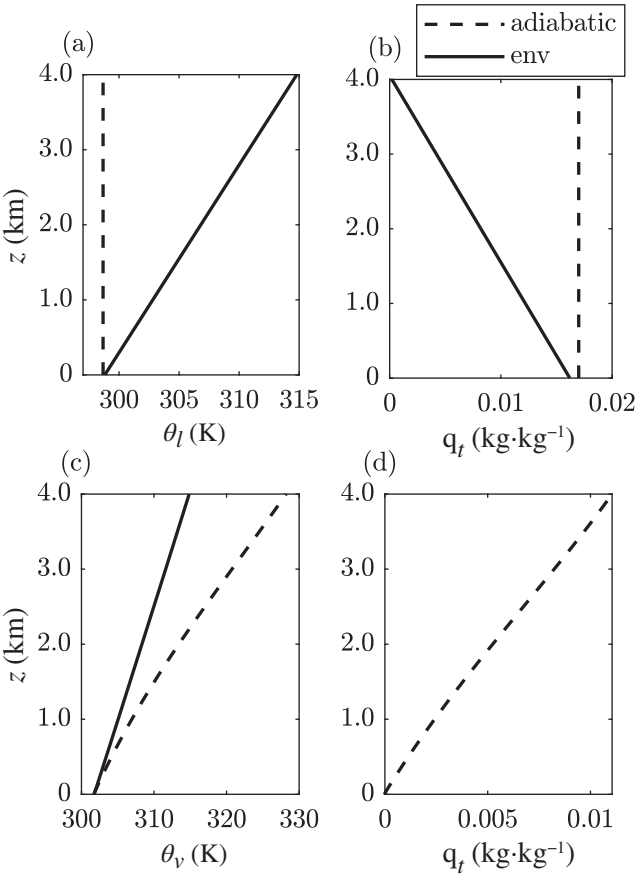

FIGURE 2 The vertical evolution of (a) the liquid water potential temperature θ_l, (b) the total specific humidity q_t, (c) the virtual potential temperature θ_v, and (d) the liquid water specific humidity q_l. Solid lines mark the values of the background environment, and dashed lines mark the evolution of the injected cloud source fluid assuming an idealised adiabatic process.

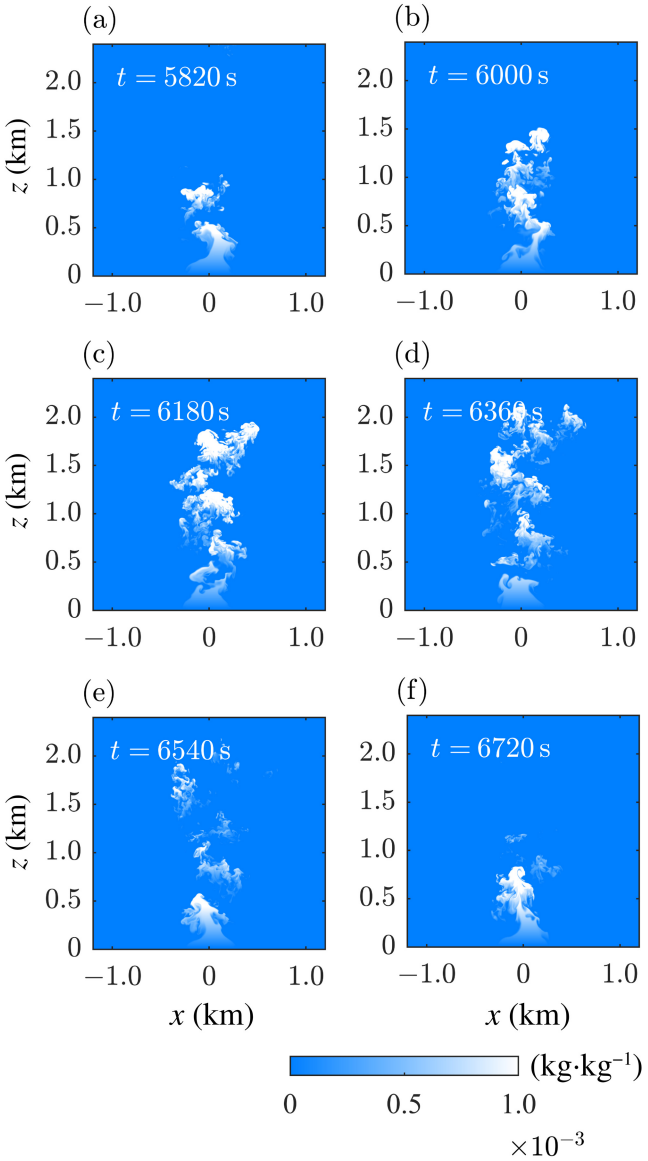

FIGURE 3 A series of snapshots of the cumulus cloud, illustrating slices through a central vertical plane with the instantaneous liquid water specific humidity field, q_l highlighted. The snapshots are equally spaced in time within the time period $t = 5,820$–$6,720$ s; that is, throughout the statistically steady state.

width (see Figure 3). Our results, therefore, can be considered not to be contaminated by interactions with the top and sides of the domain.

In order to be able to achieve a statistically steady state, cloud conditioning is avoided by defining some nudging regions near the outer edges of the domain, in which we nudge the properties of the fluid to the prescribed conditions of the background environment: at radial distances larger than $8r_0 = 2,000$ m from the injection point (the light blue shade in Figure 1), the liquid water potential temperature and total water specific humidity are forced back to the background environmental values using a time-scale of 360 s. The background environmental properties (i.e., $\theta_{v,e}$) are calculated as a horizontal mean over this nudging area. To be concise, hereafter, we omit "background" when referring to the background environmental properties; that is, the (background) environmental virtual potential temperature $\theta_{v,e}$. For a large enough simulation domain (as we did, see discussion on Figure 6a), the calculated environmental properties using this nudging area should be close to the values prescribed in Figure 2. To avoid the reflection of internal waves at the top, a nudging area 100 m in height is set covering the ceiling to nudge the local w to zero (the grey shade in Figure 1). Periodic boundary conditions are applied on the sidewalls of the domain, and Neumann boundary conditions for both velocity and buoyancy are applied at the domain top. At the domain bottom, a Neumann boundary condition is applied

for buoyancy and a free slip boundary condition for velocity, apart from the injection region, which uses Dirichlet boundary conditions.

A fully parallelised code for direct and large-eddy simulation, SPARKLE, is used to solve Equations 3–10 on a uniform Cartesian grid of $N_x \times N_y \times N_z = 2,560^3$ cells. SPARKLE uses a fourth-order accurate spatial discretisation and a third-order variable time step Adams–Bashforth time-integration scheme in time. Details of the numerical method used in SPARKLE can be found in Craske and Van Reeuwijk (2015). The Reynolds number of the simulated cloud is $Re = UL/\nu = 30,000$, where the characteristic velocity $U = 1\,\mathrm{m}\cdot\mathrm{s}^{-1}$ and length $L = 3,000\,\mathrm{m}$ are estimated from the averaged vertical velocity and total height of the updraught that will be shown in Figure 6a,f. The source Reynolds number of the cloud is $Re_s = w_m r_0/\nu = 2,000$. The simulation was run for a duration of 10,800 s in order to allow sufficient time for the cloud to reach a statistically steady state.

Local instantaneous data (e.g., $q_l(\boldsymbol{x}, t)$) were obtained at intervals of 60 s. Once the cloud reached a statistically steady state, results were quasi-steady and azimuthally symmetric (here, axisymmetric in x and y). Azimuthally Reynolds-averaged data $\overline{\chi}(r,z)$, where χ is an arbitrary variable, were collected by partitioning the domain into concentric cylindrical shells (see Figure 1 for the coordinate) and averaging over all cells lying within a given shell (Craske & Van Reeuwijk, 2015; Van Reeuwijk, & sallizoni P, Hunt G, Craske J., 2016). Conditional statistics were obtained for two flow regions: (1) the cloud region (where the air contains liquid water or is cloudy, hereafter denoted by a subscript "cld"), and (2) the cloud updraught region (the rising part within the cloud region, hereafter denoted by a subscript "up"). The time-averaged statistics of the regions were obtained within the statistically steady state.

3 | CLOUD OBSERVATIONS AND CLOUD REGIONS

3.1 | Instantaneous flow

Snapshots of the instantaneous liquid water specific humidity q_l on an x–z plane through the centre of the domain over the entire simulation time are taken and can be found as an animation online. From these snapshots, we observe extreme cyclic behaviour of the cloud, which we describe here and return to in Section 3.2. This is consistent with the observations in French *et al.* (1999); Zhao and Austin (2005); Heus *et al.* (2009).

Figure 3 shows one cycle of this cyclic behaviour at six times between $t = 5,820$ s and $6,720$ s. At around $t = 5,820$ s, a cloud is about to rise; the bright white at the cloud front indicates large condensation of the water and associated heat release that will fuel the cloud development. In the subsequent snapshots, Figure 3b–e, this cloud grows to a maximum height and gradually dissipates due to evaporation at around $t = 6,540$ s. Apart from the bright white regions representing the cloud core, evaporation can be observed by the residual light white on the cloud edges and the disconnected regions from the cloud core. At around $t = 6,720$ s, the cloud has nearly disappeared, and the next cloud cycle can subsequently start. Throughout the simulation duration, this quasi-periodic process occurs cyclically due to the imposed steady source conditions and forms a series of clouds.

Visualisation of data (e.g., see the animation included online) shows that, when an upcoming pulse is about to rise (e.g., the instant shown in Figure 3f), the saturated fluid appears to pause its rise at around $z \approx 0.5$ km, before overshooting this level and then forming an active cloud. By examining individual clouds within an LES of a cloud ensemble, Heus *et al.* (2009) reported that the cyclic extreme pulses are an intrinsic nature of shallow cumulus clouds independent from the sub-cloud layer (the layer below the cloud base where the unsaturated air mixes to form the condition of the cloud base) but could be related to the convective inhibition region (the thin atmospheric layer above the cloud base in which the cloud is locally negatively buoyant). Our simulations evidence that the pulses are independent from the sub-cloud layer, since we do not set a sub-cloud layer. However, we do not set a convective inhibition region either within the simulation configuration (see Figure 2c). Finally, we note that turbulent single-phase fountains in stratified environments do show such cyclic pulsing behaviour (see, e.g., Bloomfield & Kerr, 2000; Ansong *et al.*, 2008) but that the cyclic behaviour of these flows is not as extreme as that of shallow cumulus clouds—this might suggest that it is the phase change of the water (evaporation and condensation) that plays a dominant role in the extreme cyclic nature of these clouds.

The interaction between the previous pulses and forthcoming pulses is noteworthy since the physics of the cloud pulse evaporation can have different, either enhancing or suppressing, effects on forthcoming pulse formation. On the one hand, the previous cloud cycles have moistened and cooled the air, thereby providing an environment that is more favourable to the formation and development of any forthcoming pulse (Heus *et al.*, 2009); on the other hand, as the previous cloud pulse evaporates, it leaves environmental fluid that is negatively buoyant (locally), which then acts as counterflow within the environment, thereby suppressing the rising forthcoming rising pulse. This second effect can be investigated from Figure 4, which plots

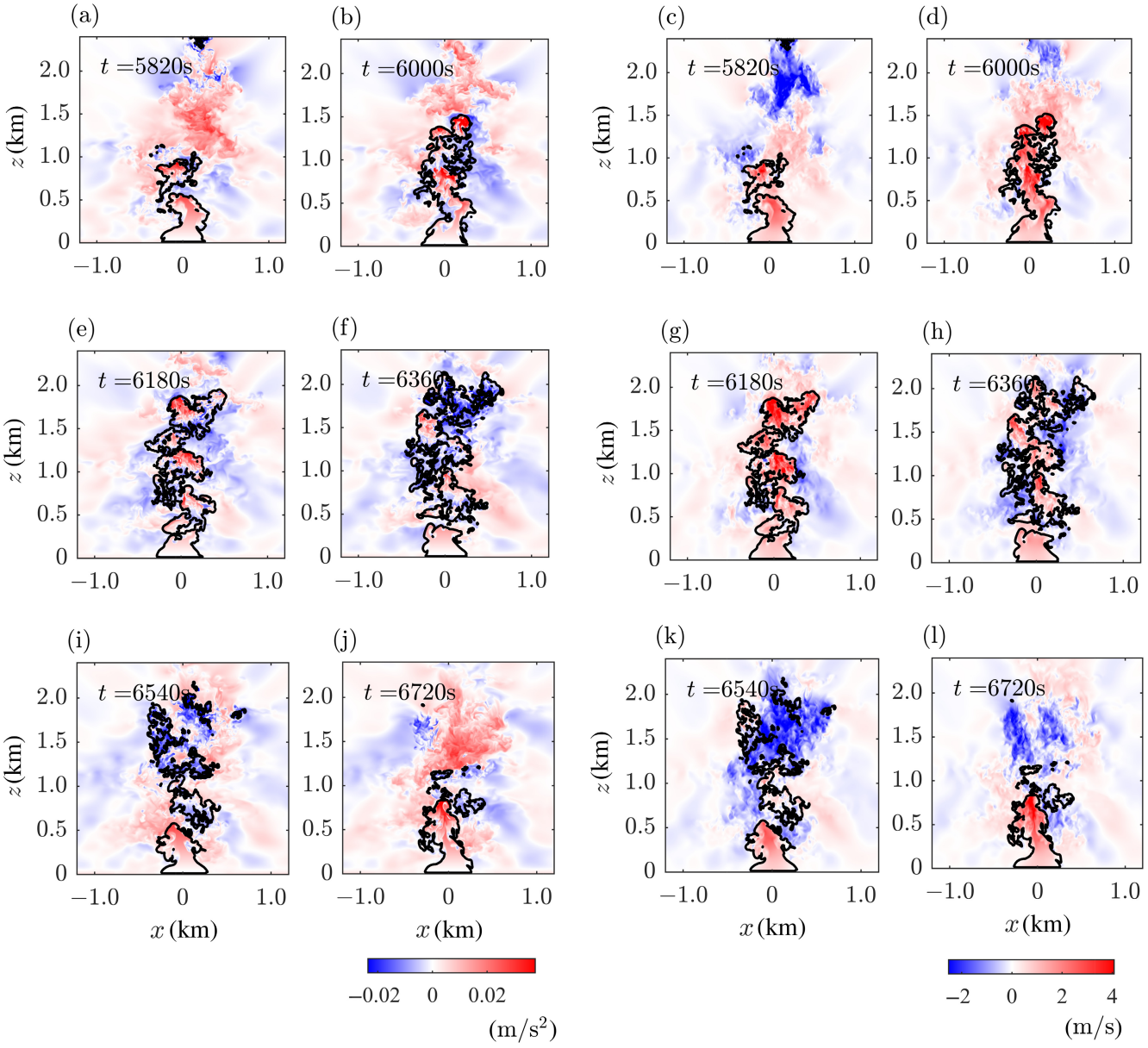

FIGURE 4 Twelve snapshots illustrating data on the central vertical plane at six different instants: (a,b,e,f,i,j) data for the instantaneous buoyancy field b; (c,d,g,h,k,l) data for the vertical velocity field w. Overlaid as a black line in each is the cloud boundary (defined by an isosurface of liquid water specific humidity $q_l = 0$); data for liquid water specific humidity at the same six instants were shown in Figure 3.

vertical cross-sections of instantaneous buoyancy b fields and vertical velocity w fields. Within the figure, the cloud boundary, defined by the isosurface where the instantaneous liquid water specific humidity satisfies a minimal threshold, $q_l(\boldsymbol{x}, t) = 10^{-8}\,\mathrm{kg}\cdot\mathrm{kg}^{-1}$, is highlighted by the black lines, which encompass the cloud region within it. Figure 4c,d,k,l shows patches of fluid with significant negative vertical velocities (blue regions) that have resulted from the evaporation of a previous cloud cycle (and its consequent negative buoyancy; see Figure 4f,i)—these illustrate occasions when the evaporation of a previous cloud pulse is acting to significantly suppress the next rising pulse. A quasi-steady balance between these two effects, resulting from cloud pulse evaporation, takes time to develop; we define the statistically steady state when these two opposite effects reach a balance. Although we have made every effort to promote steadiness within the simulation, the cloud displays cyclic pulsing behaviour. As a result, statistically steady metrics can only be obtained by averaging over a sufficient number of cycles. We will define this statistically steady-state period in detail in Section 3.2.

Figure 4 richly illustrates further information regarding the dynamics of these clouds. For example, in the environment far from the cloud, the presence of internal waves can be inferred from the blue and red inclined patterns, which are induced by density perturbations that were excited by the cloud. Closer to the cloud, but still outside its boundary, examination of the data shows that the flow is still turbulent due to the previous cloud dynamics (qualitative examination of Figure 4 shows that fluid outside the cloud boundary still exhibits patternations that are associated with turbulence). Although not outlined here, the locations of positive vertical velocity (e.g., Figure 4c,d,g,h,k,l) indicate that the boundary of cloud updraught might, typically, be close to the cloud boundary (outlined in black in the figure), suggesting that the subsiding shell (the region within the cloud that exhibits negative vertical velocity) can be a relatively thin region just within the instantaneous cloud boundary. During the first half of the snapshots (i.e., Figure 4a,b,e and c,d,g), large red areas are observed inside the cloud, which show the cloud is positively buoyant and rising, primarily due to the latent heat release of condensing water. By contrast, in the second half (Figure 4f,i,j,h,k,l), the blue areas inside the cloud (representing the negative buoyancy and velocity respectively) become apparent. From the time evolution of the cloud shown in the second half of the snapshots, it is apparent that the cloud gradually dissipates under evaporation, producing the observed negative buoyancy, which then acts to reverse the flow and results in the observed negative velocities. (Note that, at these same instants, the blue regions within the velocity field are typically smaller than the blue regions within the buoyancy field, e.g., Figure 4f,h, indicating the order of inverse.)

3.2 | Conditional cloud and updraught statistics

The extreme cyclic nature of the flow is shown particularly clearly when vertical variation in the in-cloud horizontally averaged liquid water specific humidity, vertical velocity, and buoyancy are plotted as a function of time t (Figure 5). The in-cloud horizontally averaged value of any variable $X = X(\boldsymbol{x}, t)$ is defined

$$X_{\mathrm{cld}}(z,t) = \frac{\int_{\Omega_{\mathrm{cld}}} X \, dA}{\hat{A}_{\mathrm{cld}}}, \quad \hat{A}_{\mathrm{cld}}(z,t) = \int_{\Omega_{\mathrm{cld}}} dA, \qquad (14)$$

where $\Omega_{\mathrm{cld}}(z,t)$ is the instantaneous region within the cloud boundary (i.e., the region for which $q_{\mathrm{l}} > 0$) and $\hat{A}_{\mathrm{cld}}(z,t)$ is the local instantaneous cloud cross-sectional area.

Figure 5a shows $q_{\mathrm{l,cld}}(z,t)$, which clearly shows a series of cloud pulses. Note that the pulses within the time $t = 5,820$ s to $t = 6,720$ s are associated with the cross-sections shown in Figure 3. The gradient of the inclined stripes illustrates the rise velocity of the cloudy air, which is approximately $1.7\,\mathrm{m}\cdot\mathrm{s}^{-1}$, on average. Based on Figure 5a, the first four pulses (e.g., before $t = 5,400$ s) have larger variations in maximum rise heights and have a slightly wider gap (the blue regions) between each other, which indicates that the interaction between the previous pulses and forthcoming pulses described earlier has not reached a balance. After $t \approx 5,400$ s the pulses have a more consistent maximum rise height and also form closer together, in time. Therefore, the time period before $t = 5,400$ s is regarded as including the effects of the simulation transients and so are disregarded in our analysis; the times 5,400–10,800 s are regarded as representative of the statistically steady state and deemed suitable for inclusion within our analysis's further time-averaged statistics.

The data plotted in Figure 5b show a time series of the vertical variation in the instantaneous in-cloud, horizontally averaged, vertical velocity w_{cld}; in these data too, the pulses can also be clearly observed. For each pulse, the negative velocities, over all the heights where they appear, tend to follow immediately after positive velocities, showing that the rising cloud eventually falls (as the result of its partial evaporation). The converse is only true low down in the cloud pulse (i.e., only when the cloud pulses are first forming do positive velocities immediately follow negative); higher up, the pulses are distinctly separate (in time), and the positive velocities of the rising pulses follow quiescent periods of near-zero vertical velocities. Note that the rise time of each pulse is typically longer than the duration of its fall. Moreover, we can observe that, at some instants, there is a negative-velocity (blue) region above a positive-velocity (red) region, evidencing that some rising cloud pulses encounter the previous falling cloud pulse.

Figure 5c shows a time series of the vertical variation in the in-cloud, horizontally averaged, buoyancy b_{cld}, which shows that for each individual pulse the buoyancy is initially positive and evolves, eventually becoming negative. However, unlike the vertical velocity, the negative buoyancy seems to persist for longer than the positive buoyancy, especially above $z \approx 500$ m; for example, compare the relative widths of the blue and red bands in Figure 5c. Examining Figure 5b,c shows that, as one might expect, the cloud fluid first becomes negatively buoyant, which then acts against the rising flow, ultimately reversing the flow, as evidenced by the subsequent negative vertical velocity. Figure 5c also shows that the maximum negative buoyancy is concentrated near the cloud top; this is due to the fact that the cloud liquid water amount is maximum near

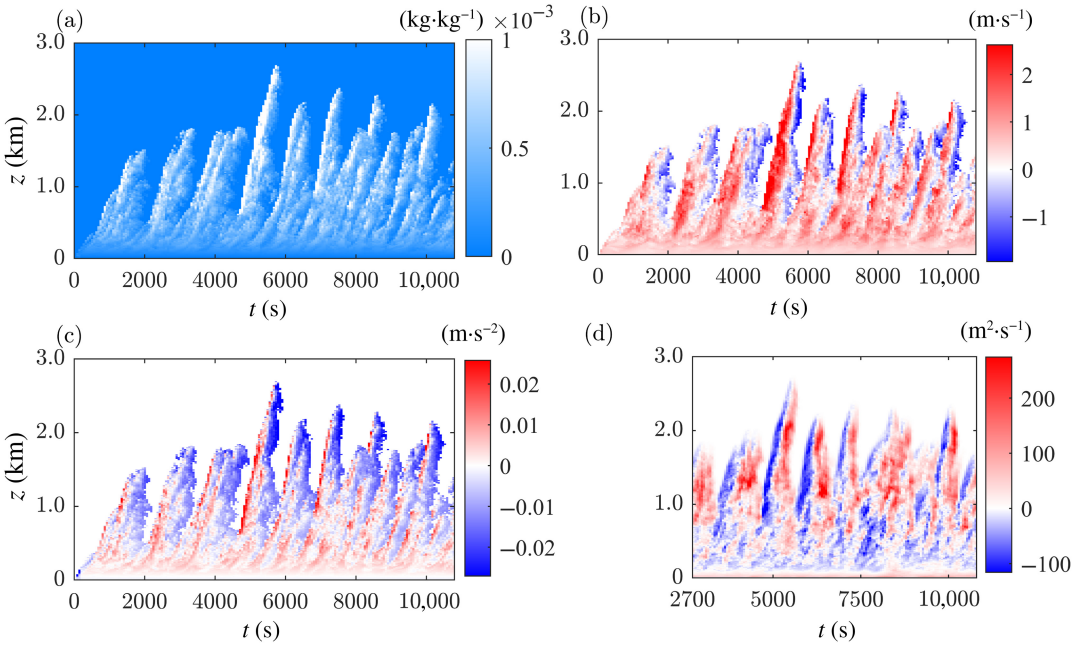

FIGURE 5 Time series plots showing the vertical variation of the in-cloud horizontally averaged conditions over time: (a) the liquid water specific humidity $q_{l,cld}$, (b) the vertical velocity w_{cld}, (c) the buoyancy b_{cld}, and (d) the net entrainment and detrainment $\hat{q}_{cld}$. The entire simulation duration is included in (a)–(c), whereas (d) only illustrates the period over which statistically steady data, relevant to entrainment, were gathered. The colour schemes in (a) follow that for the total water specific humidity in Figure 3, (b) and (c) follow that of the equivalent data in Figure 4, and in (d) the blue regions mark net entrainment and red the net detrainment; colour bars in each indicate the magnitudes associated with the data presented.

the cloud top, which gives rise to a maximum evaporative cooling potential (de Roode, 2007).

Figure 5d shows the cloud's net entrainment, or detrainment, flux per unit height, and we return to discuss this in Section 4.5.

The steady-state in-cloud statistics are explored in the following, both for in-cloud—denoted with the subscript "cld" and defined by Equation(14)—and updraught quantities (denoted with the subscript "up"), with the latter defined analogously as

$$X_{\mathrm{up}}(z,t) = \frac{\int_{\Omega_{\mathrm{up}}} X\, dA}{\hat{A}_{\mathrm{up}}}, \quad \hat{A}_{\mathrm{up}}(z,t) = \int_{\Omega_{\mathrm{up}}} dA, \tag{15}$$

where the instantaneous cloud updraught Ω_{up} is identified as the rising part of the cloud; for example, $q_l(\boldsymbol{x},t) > 0$ and $w(\boldsymbol{x},t) > 0$. Time-averaged in-cloud (horizontally averaged) and updraught quantities are determined by

$$\langle X_i \rangle(z) = \frac{\int_T X_i \hat{A}_i\, dt}{\int_T \hat{A}_i\, dt}, \tag{16}$$

where $i = \{\mathrm{cld}, \mathrm{up}\}$ and T is the duration of the time-averaging window.

Figure 6 shows the time-averaged cloud and updraught mean quantities. Figure 6a shows the time-averaged cloud updraught area and the entire cloud area. These are shown normalised by the cross-section area of the simulation domain and indicate that, over most heights, the cloud regions take less than 0.5% of the whole plane—emphasising that the far environment was not likely to be significantly affected by the clouds formed. The updraught area is typically 60–70% of the total cloud area, whereas the rest is the time-averaged subsiding shell (this is generally consistent with what we have observed from the thin negative-velocity layer near the cloud boundary in Figure 4, where the width of the cloud regions [square root of the area] is indicated at one specific plane clip at some instants); we note that this value is smaller than the 90% reported in LESs obtained from the cloud ensemble (Siebesma *et al.*, 2003). The cloud area peaks around $z \approx 800$ m; above this height, the area decreases with height as the evaporation dominates and the dissipation of the cloud becomes more significant, thereby reducing its area. The heights of both the updraught and the bulk cloud are approximately $z = 2,750$ m, with the bulk cloud slightly higher.

Figure 6b,c shows that, as a result of lateral mixing (i.e., mixing due to the processes of entrainment and detrainment), both the (horizontally averaged values of) cloud liquid water potential temperature and total water specific humidity vary significantly with height, with their values

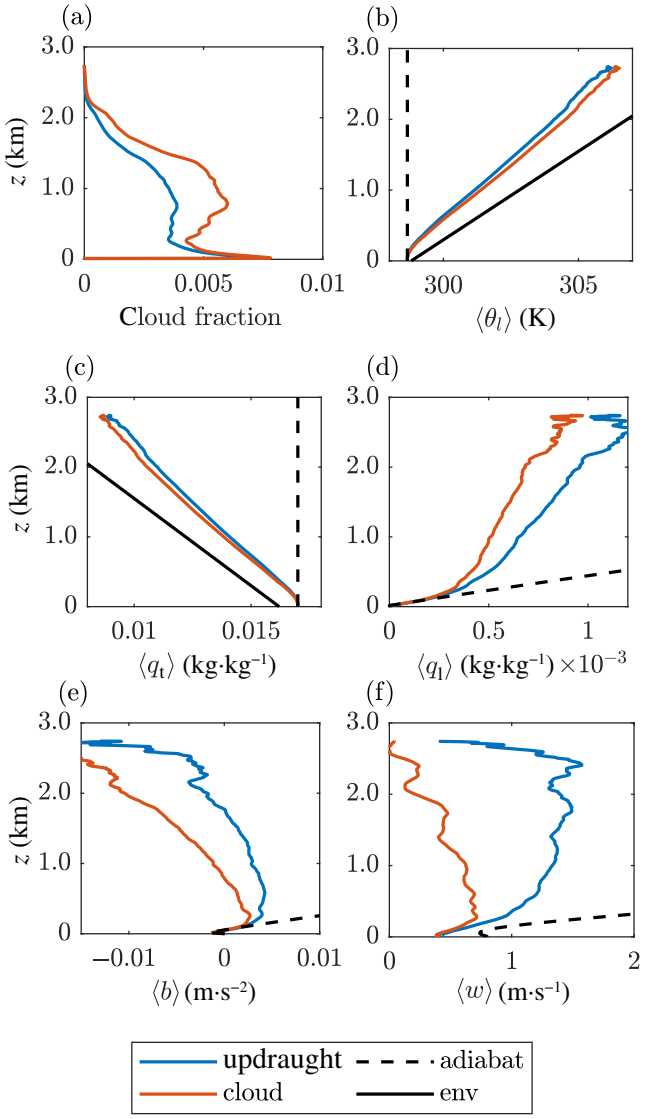

FIGURE 6 The vertical evolution of mean, horizontally averaged, properties: (a) the cloud fraction, (b) the liquid water potential temperature $\langle\theta_l\rangle$, (c) the total water specific humidity $\langle q_t\rangle$, (d) the liquid water specific humidity $\langle q_l\rangle$, (e) the buoyancy $\langle b\rangle$, and (f) the vertical velocity $\langle w\rangle$. In each, data of the updraught is depicted by a blue curve and that of the bulk cloud by a red curve. Included as dashed lines are data associated with the evolution of the source fluid under an idealised adiabatic process; the solid black lines mark the values of the background environmental fluid.

falling between the source (adiabatic) and environmental values. In each plot, the property for the updraught is close to the (bulk) cloud values, falling only slightly closer to the source value than the cloud values, suggesting that the inner updraught mixes less with the environmental air than the cloud average.

Figure 6d shows the vertical variation in the mean liquid water specific humidity. Within the figure, the idealised adiabatic process (in which evaporation is absent) is shown by the dashed line; it can be seen that, for the adiabatic process, the liquid water specific humidity grows rapidly with height as the source fluid condenses under these idealised conditions. However, the in-cloud mean and updraught mean values are much lower than those of the adiabatic process, with the total specific humidity slightly higher in the cloud updraught than in the cloud; since the updraught sits at the core of the cloud it is relatively less affected by evaporation at the cloud edges and hence exhibits slightly higher liquid water specific humidity. Figure 6e shows the mean buoyancy associated with the virtual potential temperature difference between the cloud regions and the environment. For the idealised adiabatic process, the buoyancy is strictly positive and grows monotonically with height due to the continued release of latent heat. However, with the effect of evaporative cooling included, the bulk cloud becomes negatively buoyant at about $z = 1,000$ m, with the updraught becoming negatively buoyant higher up ($z \approx 2,000$ m)—again because the updraught is relatively less affected by evaporation. The mean vertical velocity (Figure 6f) shows that the updraught accelerates up until the height $z \approx 2,200$ m, whereas the entire bulk cloud decelerates over almost all heights ($z \gtrsim 200$ m) due to evaporative cooling. Although decelerating, the bulk cloud vertical velocity remains positive over the entire cloud height, approaching zero near the top.

3.3 | Reynolds-averaged cloud statistics

Since the simulation produces statistically axisymmetric (practically in $\{x, y\}$ due to the Cartesian grid) steady data, we define the Reynolds-averaging operator (see also Craske & Van Reeuwijk, 2015; Huang *et al.*, 2023a; Van Reeuwijk, & sallizoni P, Hunt G, Craske J., 2016)

$$\overline{X}(r,z) \equiv \frac{1}{2\pi T}\int_T \int_0^{2\pi} X(r,\varphi,z,t)\, d\varphi\, dt, \qquad (17)$$

where X is an arbitrary field, $r = (x^2+y^2)^{1/2}$, and $\varphi = \tan^{-1}(y/x)$ is the azimuthal direction. Figure 7a shows data for the Reynolds-averaged liquid water specific humidity $\overline{q_l}(r,z)$. Consistent with the criterion of the instantaneous cloud, the Reynolds-averaged cloud is identified by the Reynolds-averaged cloud boundary defined by the radial location r_{cld}, beyond which $\overline{q_l} > 0$. The figure indicates that the Reynolds-averaged cloud height is approximately 2, 750 m.

The magnitude of Reynolds-averaged total water specific humidity $\overline{q_l}$ is generally lower than the instantaneous q_l field (note that the magnitudes on the colour bar of Figure 7a relative to Figure 3). Furthermore, in the Reynolds-averaged field, the large magnitude is

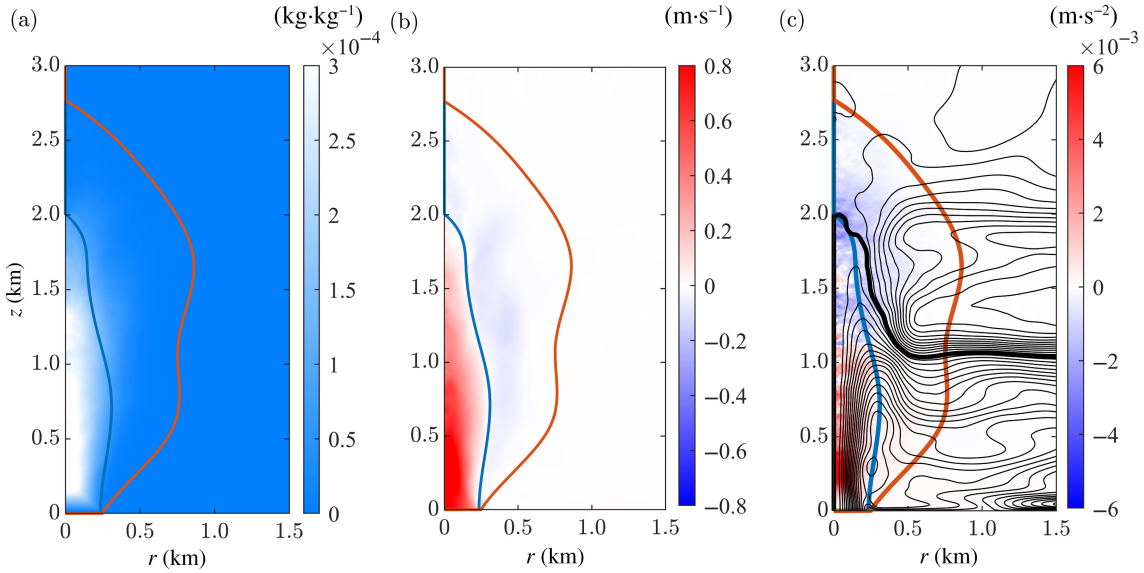

FIGURE 7 The (azimuthally) Reynolds-averaged fields of: (a) the liquid water specific humidity $\overline{q_l}$, (b) the vertical velocity $\overline{w}$, and (c) the net force acting on the cloud $\overline{b} - d\overline{p}/dz$. Overlaid are the Reynolds-averaged cloud boundary (marked by the red curve) and Reynolds-averaged cloud updraught boundary (marked by the blue line). The solid black lines in (c) are the velocity streamlines, with the separatrix originating from the centre of the source highlighted in bold.

concentrated near the cloud centre line. These differences occur primarily due to the extreme intermittency of the cloud and its effects on the different averaging processes (Lenderink *et al.*, 2004; Siebesma, 1998). As discussed in the previous sections (see Figures 3 and 5), the cloud is only present a certain percentage of the time at a particular radius and height; therefore, when taking the simple time average (e.g., within the Reynolds average) over the whole history, the magnitude of time-averaged properties (e.g., the $\overline{q_l}$ and $\overline{w}$) will be "diluted" by intermittent observations that reflect properties of the environmental fluid. Since the probability of having a cloud is largest near the cloud centre line, one expects that, for example, $\overline{q_l}$ will be largest near the centre line.

The intermittency also influences the Reynolds-averaged cloud boundary (i.e., based on $\overline{q_l}$). For the conditional statistics, the $q_l > 0$ criterion encloses the instantaneous cloudy area. However, since, at most locations, $\overline{q_l}$ includes an average of instants when any given location is within the cloud and those when the location is outside the cloud, the Reynolds-averaged cloud boundary, defined by the threshold $\overline{q_l} > 0$, contains all locations that have ever been cloudy. Thus, the Reynolds-averaged cloud boundary encompasses a much larger volume than the equivalent conditionally averaged cloud does, as visible by comparing Figures 7 and 6a.

Figure 7b plots the Reynolds-averaged vertical velocity field $\overline{w}(r, z)$. The cloud updraught radius r_{up} is identified based on the loci of outermost points satisfying both $\overline{q_l} > 0$ and $\overline{w} > 0$. Because the updraught is near the cloud centre line, and therefore less affected by the evaporative intermittency, the width of the Reynolds-averaged updraught is relatively similar to that obtained from the conditional statistics (see Figure 4). In the Reynolds-averaged framework, the region encompassed by the cloud boundary r_{cld} and the cloud updraught radius r_{up} encompasses locations at which the cloud is only intermittently present. This is distinctly different to definitions based on the instantaneous locations of these boundaries, and hence the width and shape of this region differ significantly between the Reynolds-averaged and conditionally averaged frameworks. Moreover, at locations within the Reynolds-averaged cloud boundary r_{cld} and the cloud updraught radius r_{up}, when the cloud is absent the velocities can be significant and varied. Hence, we hereafter choose not to term the region between r_{up} and r_{cld} as the "subsiding shell", terminology widely used within the conditional analysis of LES data; instead, we term this region the "downdraught".

Figure 7c shows the streamlines associated with the steady state; they were derived by calculating the stream function associated with the velocity field and plotting isosurfaces of this stream function. Thus, the volume flux between each adjacent pair of streamlines, a stream tube, is constant and equal for all stream tubes. These streamlines highlight many interesting features of the flow. First, we note the presence of a separatrix (highlighted in the figure by the thick black line), which separates the fluid injected from the cloud base from the flow induced by turbulent entrainment and evaporative cooling at the cloud

top. Second, we observe an outflow region at $z \approx 1,000$ m (highlighted by the separatrix within this region), which implies that the average virtual potential temperature resulting from the mixing inside the cloud is equal to the environmental virtual potential temperature at that level, which is typically referred to as the neutral buoyancy level. The outflow region shows a concentration of stream tubes over a height of about 300 m, implying a large net detrainment zone at that height. The figure shows that the Reynolds-averaged cloud net entrains air from about 2.0 km height, which then mixes and descends together with the in-cloud air to its neutral buoyancy level just above the separatrix. Conversely, the fluid injected from the source rises up to a maximum height of about 2.0 km, after which it descends, once again due to evaporative cooling, until it detrains from the cloud just below the separatrix. Third, there are closed streamlines that sit across the updraught boundary, in the region $z \approx 300$–600 m, which show that (in a Reynolds-averaged sense) a small portion of the fluid net detrains from the updraught and then descends and is then re-entrained once more into the updraught. However, over most heights of the updraught (e.g., $z > 600$ m), the updraught net detrains fluid into the downdraught and further detrains out of the cloud. Fourth, note that a few streamlines very close to the injection point at the edge of the source (at $r \approx 250$ m, $z = 0$) immediately return to the bottom and then detrain horizontally. This is because the fluid at the edge of the source immediately mixes with the environment, leading to evaporation, and thus net detrainment occurs of the updraught and cloud at the very bottom of the domain. We note that the streamlines of the cloud updraught are generally consistent with the observations of Peters *et al.* (2020); Morrison *et al.* (2020), who also reported net entrainment in the lower portion of the updraught and net detrainment higher up. These inferences were made by investigating the velocity vectors of the updraught in a relatively humid environment in LES.

The coloured background in Figure 7c indicates the local value of net force arising from the Reynolds-averaged vertical momentum equation; that is, $\overline{b} - d\overline{p}/dz$. This net force is expected to be zero in regions where the flow is in a hydrostatic balance. There is a strong net upward forcing below 1.0 km, clearly evidenced by the red region there. This arises due to the provision of latent heat from condensation. Conversely, a net downward force is evidenced higher up by the blue region within the figure—this arises due to evaporative cooling. Note that the streamlines only present the mean flow dynamics, whereas the turbulent transport is not directly visible in the figure. This turbulent transport is important in a number of aspects; for example, turbulence acts to transport vertical momentum across the streamlines, particularly above 1.0 km.

4 | ENTRAINMENT AND DETRAINMENT STATISTICS

To first investigate the "net" entrainment and detrainment statistics of the cloud, the conservation equations for the cloud updraught, downdraught, and entire cloud are presented in both the Reynolds-averaged and conditionally averaged framework, starting with the Reynolds-averaged approach. Note that to enable comparison with the existing analysis of equivalent single-phase flows (see Huang *et al.*, 2023a, 2023b), we define the entrainment as the volume flux that flows into the cloud region per height (e.g., Equations 20 and 29); doing so is slightly different from the LES convention, where this entrainment is additionally scaled by the local cloud area; see Equations 1 and 2.

4.1 | Reynolds-averaged shallow cumulus clouds

Based on the Reynolds-averaged cloud and updraught boundaries r_{up} and r_{cld} (see Figure 7), the cloud updraught is defined to be the region from $r = 0$ to $r = r_{\mathrm{up}}$, and the downdraught (denoted by "down") to be the region from $r = r_{\mathrm{up}}$ to $r = r_{\mathrm{cld}}$. The Reynolds-averaged vertical volume fluxes associated with the updraught and downdraught regions are respectively defined as

$$Q_{\mathrm{up}}(z) \equiv 2\int_0^{r_{\mathrm{up}}} \overline{w} r \, dr \quad \text{and} \quad Q_{\mathrm{down}}(z) \equiv 2\int_{r_{\mathrm{up}}}^{r_{\mathrm{cld}}} \overline{w} r \, dr. \tag{18}$$

Note that a factor π is omitted from these integrals for consistency with the analysis of single-phase flows (e.g., Huang *et al.*, 2023a; Morton *et al.*, 1956; Van Reeuwijk, & sallizoni P, Hunt G, Craske J., 2016). The associated Reynolds-averaged conservation equations can be obtained by writing the continuity equation, Equation (3), in cylindrical coordinates and integrating over the region from $r = 0$ to $r = r_{\mathrm{up}}$ for the updraught region, and the region from $r = r_{\mathrm{up}}$ to $r = r_{\mathrm{cld}}$ for the downdraught region, with the result

$$\frac{dQ_{\mathrm{up}}}{dz} = -q_{\mathrm{up}}, \quad \frac{dQ_{\mathrm{down}}}{dz} = q_{\mathrm{up}} - q_{\mathrm{cld}}, \tag{19}$$

where q_{up} and q_{cld} are the perpendicular exchanges of volume across the updraught and cloud boundary respectively. These are defined

$$\begin{aligned} q_{\mathrm{up}}(z) &= 2r\left(\overline{u}_{\mathrm{r}} - \overline{w}\frac{dr}{dz}\right)\Big|_{r_{\mathrm{up}}}, \\ q_{\mathrm{cld}}(z) &= 2r\left(\overline{u}_{\mathrm{r}} - \overline{w}\frac{dr}{dz}\right)\Big|_{r_{\mathrm{cld}}} \end{aligned} \tag{20}$$

and are termed "net entrainment" or "net detrainment" fluxes depending on the direction of the fluxes and one's perspective when describing the flow from that of a particular flow region (see later for an example). The term $\overline{u}_r$ is the radial velocity, and the term associated with the radial change, dr/dz, is the Leibniz term within the integral.

We take this opportunity to make three points that are intended to be helpful when interpreting the results. First, the signs before q_{up} in Equation (19) indicate that, here, a flux in the negative radial direction (i.e., negative q_{up}) increases the volume flux within the updraught Q_{up} and decreases the volume flux downdraught Q_{down}, with the opposite true for fluxes in the positive radial direction. Similarly, a flux in the negative radial direction entraining across the cloud boundary (i.e., a negative q_{cld}) contributes positively to the downdraught volume flux Q_{down}—see Equation (19); the opposite is true for detrainment. Therefore, a negative q_{up} (q_{cld}) represents the net entrainment into the updraught (cloud), whereas a positive q_{up} (q_{cld}) represents the net detrainment out of the updraught (cloud).

Second, the rightmost equation in Equation (19) shows that the downdraught region simultaneously exchanges volume flux (entrains or detrains) via both edges; that is, the updraught boundary and the cloud boundary. By definition, the vertical velocity $\overline{w}$ is positive within the updraught and negative within the downdraught; hence, Q_{down} is negative. The volume flux of the entire cloud region is defined as $Q_{cld} = Q_{up} + Q_{down}$, with positive values representing net upward volume fluxes within the cloud; and combining both equations in Equation (19) results in

$$\frac{dQ_{cld}}{dz} = -q_{cld}. \tag{21}$$

Third, entrainment and detrainment may, at any given location on the boundaries, occur intermittently. This potentially important information is lost by taking the time average within the Reynolds-averaging process; as such, note that q_{up} and q_{cld} represent only the "net" entrainment or detrainment.

Figure 8a shows the variation with height of the Reynolds-averaged vertical volume flux of the updraught, downdraught, and the entire cloud. Consistent with Figure 7b, the updraught volume flux Q_{up} grows slightly below $z \approx 600$ m and then gradually approaches zero (at around $z \approx 1,700$ m) due to the decrease in the area and the typical vertical velocity of the updraught. However, examining from the downdraught in the direction of its flow (i.e., the negative z direction), the downdraught flux Q_{down} increases from the cloud top to about the cloud half-height and then decreases towards zero at the cloud base. As a result, the superposition Q_{cld} is positive below $z \approx 1,000$ m and becomes negative above.

Figure 8c shows the Reynolds-averaged net entrainment and detrainment of the updraught q_{up} and the entire cloud q_{cld}. These have been qualitatively discussed based on inferences from the streamlines (Section 3.3 and Figure 7c) but can now be examined quantitatively. The flux q_{up} is generally positive at most heights, with the exception of slightly negative values occurring below $z \approx 500$ m. This suggests that the updraught primarily net detrains into the downdraught across the updraught boundary. The flux q_{cld} is generally positive below $z \approx 1,300$ m, whereas it is generally negative above, suggesting there is a net detrainment from the cloud into the environment in about the lower half of the cloud and net entrainment into the cloud from the environment in the upper half. The maximum net detrainment and entrainment occur near $z \approx 1,100$ m and $z \approx 2,000$ m respectively, consistent with the region where the density of streamlines is largest (see Figure 7c).

4.2 | Conditionally averaged shallow cumulus clouds

Following Van Reeuwijk *et al.* (2021); Huang *et al.* (2023b), the statistics associated with a conditionally averaged view of the shallow cumulus cloud simulated within our digital cloud chamber are now investigated. We define the instantaneous vertical volume flux of the updraught $\hat{Q}_{up}$ and the downdraught $\hat{Q}_{down}$ (per unit π) respectively as

$$\hat{Q}_{up}(z,t) = \frac{1}{\pi}\int_{\Omega_{up}} w\, dA \quad \text{and} \quad \hat{Q}_{down}(z,t) = \frac{1}{\pi}\int_{\Omega_{down}} w\, dA, \tag{22}$$

where $\Omega_{up}(z,t)$ is the instantaneous updraught region, defined as $q_l(\boldsymbol{x},t) > 0$ and $w(\boldsymbol{x},t) > 0$ (see Section 3.1), and $\Omega_{down}(z,t)$ is the instantaneous downdraught, defined as $q_l(\boldsymbol{x},t) > 0$ and $w(\boldsymbol{x},t) < 0$. The downdraught is akin to the cloud's "subsiding shell" described in LES studies of these clouds (e.g., Heus & Jonker, 2008; Jonker *et al.*, 2008), but for consistency with our Reynolds-average analysis (Section 3.3) we again refer to this as the downdraught (using the subscript "down" to denote this region). We note that the partitioning of the cloud regions for the conditionally averaged analysis is consistent with that of the Reynolds-averaged analysis, including the definition of the conditionally averaged volume flux within the entire cloud region; that is, $\hat{Q}_{cld} = \hat{Q}_{up} + \hat{Q}_{down}$. The instantaneous conservation equations for the volume flux of the updraught and the downdraught can be obtained by integrating the

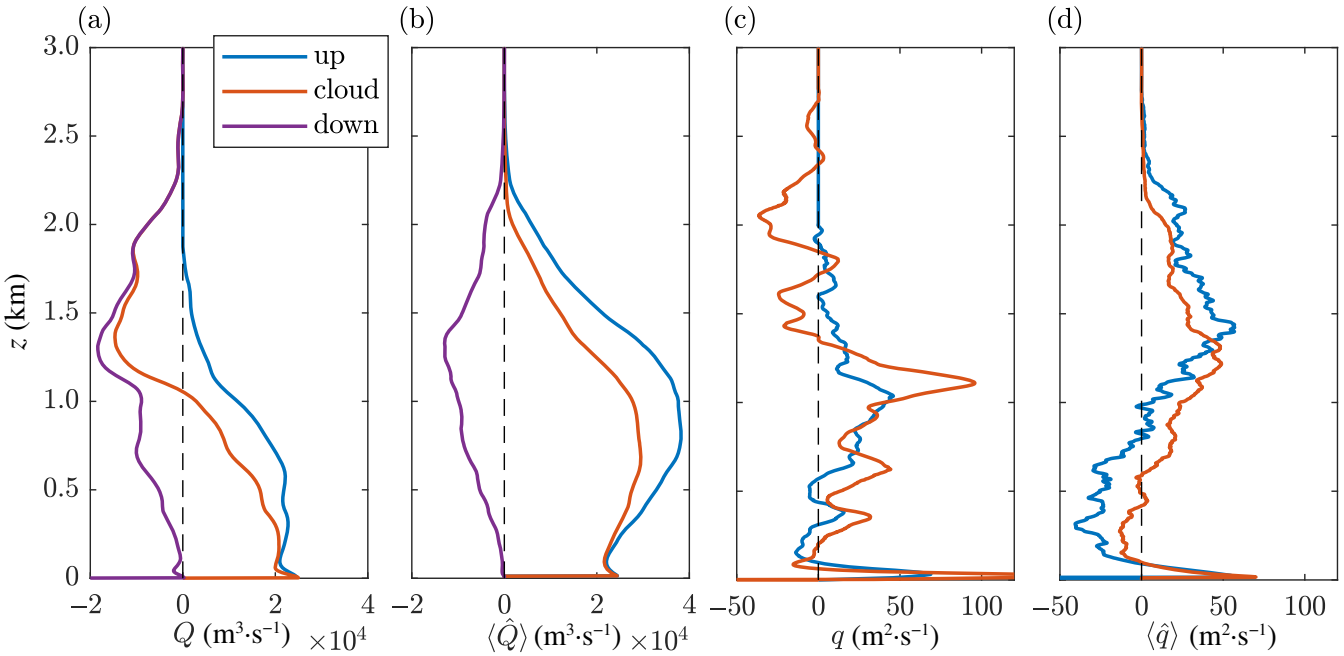

FIGURE 8 The vertical evolution within the cloud of (a) the Reynolds-averaged vertical volume flux Q and (b) the conditionally averaged vertical volume flux $\langle\hat{Q}\rangle$ within the updraught (blue curve), entire cloud (red curve), and the downdraught (purple curve). Positive values of the volume flux represent an upward transport, whereas negative values represent a downward flow. The vertical evolution at the boundaries of (c) the Reynolds-averaged net entrainment q and (d) the conditionally averaged net entrainment $\langle\hat{q}\rangle$; the blue curves mark data at the updraught boundary and the red curves mark data at the cloud boundary—negative values represent radially inward entrainment and positive values represent detrainment.

continuity equation, Equation (3), over the instantaneous updraught and downdraught region respectively, with the result (see Huang *et al.*, 2023b; Siebesma *et al.*, 2003; Van Reeuwijk *et al.*, 2021) being

$$\frac{\partial \hat{A}_{\text{up}}}{\partial t} + \frac{\partial \hat{Q}_{\text{up}}}{\partial z} = -\hat{q}_{\text{up}} \quad \text{and} \tag{23}$$

$$\frac{\partial \hat{A}_{\text{down}}}{\partial t} + \frac{\partial \hat{Q}_{\text{down}}}{\partial z} = \hat{q}_{\text{up}} - \hat{q}_{\text{cld}}. \tag{24}$$

The hat symbols denote instantaneous integral properties; that is, area integrals without any time averaging. As such, the terms $\hat{q}_{\text{up}}$ and $\hat{q}_{\text{cld}}$ represent the instantaneous "net" entrainment or detrainment across the corresponding boundaries, and the determination of the direction of $\hat{q}_{\text{up}}$ and $\hat{q}_{\text{cld}}$ is identical to the equivalent within the Reynolds-averaged framework; see earlier for a complete description. Within the conditionally averaged framework, the areas associated with the updraught and downdraught regions are respectively defined as

$$\hat{A}_{\text{up}}(z,t) = \frac{1}{\pi}\int_{\Omega_{\text{up}}} dA \quad \text{and}$$
$$\hat{A}_{\text{down}}(z,t) = \frac{1}{\pi}\int_{\Omega_{\text{down}}} dA. \tag{25}$$

Taking the time average of Equations 23 and 24 (defined $\langle X\rangle = (1/T)\int_T X\,dt$, where T denotes a suitably long time period, in our case the duration over which we gathered statistically steady data) results in

$$\frac{d\langle\hat{Q}_{\text{up}}\rangle}{dz} = -\langle\hat{q}_{\text{up}}\rangle, \quad \frac{d\langle\hat{Q}_{\text{down}}\rangle}{dz} = \langle\hat{q}_{\text{up}}\rangle - \langle\hat{q}_{\text{cld}}\rangle. \tag{26}$$

Figure 8b shows the vertical variation of the conditionally averaged volume fluxes of the updraught, downdraught, and the entire cloud. Comparing these with the Reynolds-averaged equivalents (see Figure 8a), it is surprising to note that the volume fluxes within the downdraught from both forms of analysis are almost the same; it is not obvious why this need be the case, since the area of the downdraught in the Reynolds-averaged analysis is much larger than that from the conditional average. Conversely, the volume flux of the conditionally averaged updraught is much greater than that of the Reynolds average; here, we have observed that the areas of the updraught from both statistics are broadly similar, which suggests the typical characteristic vertical velocity is greater in the conditionally averaged updraught as the intermittency dilutes the Reynolds-averaged velocity. The difference in updraught volume fluxes between the two frameworks of analysis results in the volume fluxes within the entire

cloud differing too, especially above $z \approx 1,000$ m. Unlike the Reynolds-averaged volume flux, the conditionally averaged volume flux is positive at all heights, consistent with the positive in-cloud, horizontally averaged, vertical velocity (Figure 6g).

Figure 8d shows conditionally averaged net entrainment across the boundaries, $\langle \hat{q}_{\text{up}} \rangle$ and $\langle \hat{q}_{\text{cld}} \rangle$. Different from the Reynolds-averaged q_{up}, the conditionally averaged flux $\langle \hat{q}_{\text{up}} \rangle$ exhibits negative values in the region $z \lesssim 1,000$ m, suggesting the updraught net entrains (from the downdraught) within this lower region; above this, similar to Reynolds-average q_{up}, the conditionally averaged flux $\langle \hat{q}_{\text{up}} \rangle$ indicates that the updraught exhibits net detrainment. The conditionally averaged flux $\langle \hat{q}_{\text{cld}} \rangle$ increases with height, changing from negative to a positive and peaks at $z \approx 1,250$ m before decreasing towards zero at the cloud top. This suggests that the conditional cloud net entrains from the environment below $z \approx 500$ m but net detrains above that with a maximum net detrainment at $z \approx 1,250$ m. Lastly, note that, for all four fluxes in Figure 8c,d, there is a very short positive range just above the source (i.e., over $0 \leq z \lesssim 50$ m). This is due to the net detrainment of the fluid injected from the edge of the source; this has been noticed by the streamlines (Figure 7c) from the source edge and explained at the end of Section 3.3—this impacts only a very small region at the bottom of the simulation domain and is not expected to significantly impact any of our findings.

To summarise, the Reynolds-averaged and conditionally averaged statistics provide two distinctive perspectives on entrainment. The Reynolds-averaged viewpoint provides global information about the cloud behaviour averaged over several cycles. This viewpoint clearly shows the ent km height (Figures 7c and 8c). The updraught predominantly detrains with a maximum around the neutral buoyancy level (1 km). The conditionally averaged statistics provide local information about the fluxes across the interface. It shows that, locally, there is a net entrainment into the updraught below 1 km and net detrainment above this level. The conditionally averaged cloud interface can be seen to primarily detrain fluid, presumably because of the evaporation that takes place at the cloud edge.

4.3 | Independent statistics of entrainment and detrainment

Analysis of the (instantaneous) conditional statistics provides that the individual entrainment, and the detrainment, across a given flow boundary can be decomposed and independently analysed based on the sign of the instantaneous pointwise entrainment velocity, yielding new insights to complement the net exchange across the boundary. Herein, we employ a framework introduced in Huang *et al.* (2023b) to calculate the conditional entrainment and detrainment fluxes. The instantaneous exchange across the cloud boundary can be expressed as the integral of instantaneous entrainment velocity $V_n(\boldsymbol{x}, t)$ (this being the difference between the fluid velocity and cloud boundary velocity) over the cloud boundary $\partial\Omega_{\text{cld}}$; that is,

$$\hat{q}_{\text{cld}}(z,t) = \frac{1}{\pi} \int_{\partial\Omega_{\text{cld}}} \frac{V_n}{|\boldsymbol{N}_\perp|}\, dl, \tag{27}$$

where $\boldsymbol{N}_\perp$ is the horizontal component of the normal vector of the cloud boundary to account for the entrainment perpendicular to the boundary. The entrainment velocity V_n is measured according to the cloud indicator—namely, the instantaneous liquid water specific humidity field $q_{\text{l}}(\boldsymbol{x}, t)$:

$$V_n = -\frac{1}{|\nabla q_{\text{l}}|} \frac{Dq_{\text{l}}}{Dt}, \tag{28}$$

where $D/Dt = \partial/\partial t + \boldsymbol{u} \cdot \nabla$ is the material derivative. The sign of entrainment velocity V_n identifies the regions of the cloud boundary which, at any instant, are experiencing entrainment and which are experiencing detrainment (negative values—e.g., radially inwards flow—indicating entrainment and positive values indicating detrainment). The conditional entrainment and conditional detrainment exchanges can then be respectively written as

$$\begin{aligned} \hat{q}^{-}_{\text{cld}}(z,t) &= \frac{1}{\pi} \int_{\partial\Omega^{-}_{\text{cld}}} V_n\, dl \quad \text{and} \\ \hat{q}^{+}_{\text{cld}}(z,t) &= \frac{1}{\pi} \int_{\partial\Omega^{+}_{\text{cld}}} V_n\, dl. \end{aligned} \tag{29}$$

The boundaries $\partial\Omega^{-}_{\text{cld}}(z,t)$ and $\partial\Omega^{+}_{\text{cld}}(z,t)$ are regions along the cloud boundary where $V_n < 0$ and $V_n > 0$ respectively. By definition, the net entrainment satisfies $\hat{q}_{\text{cld}} = \hat{q}^{-}_{\text{cld}} + \hat{q}^{+}_{\text{cld}}$. For tractability, the line integral, Equation (29), is re-expressed as a surface integral by applying a masking function identifying the cloud boundary (see Yurtoglu *et al.*, 2018; Huang *et al.*, 2023b, for more details).

4.4 | Entrainment and detrainment parametrisation

The conditionally segregated cloud entrainment $\langle \hat{q}^{-}_{\text{cld}} \rangle$ and detrainment $\langle \hat{q}^{+}_{\text{cld}} \rangle$ that underlie the net $\langle \hat{q}_{\text{cld}} \rangle$ are shown in Figure 9. Entrainment and detrainment coexist at the cloud boundary, and they are correlated: both peak around the half-height of the cloud. The coloured bands show one

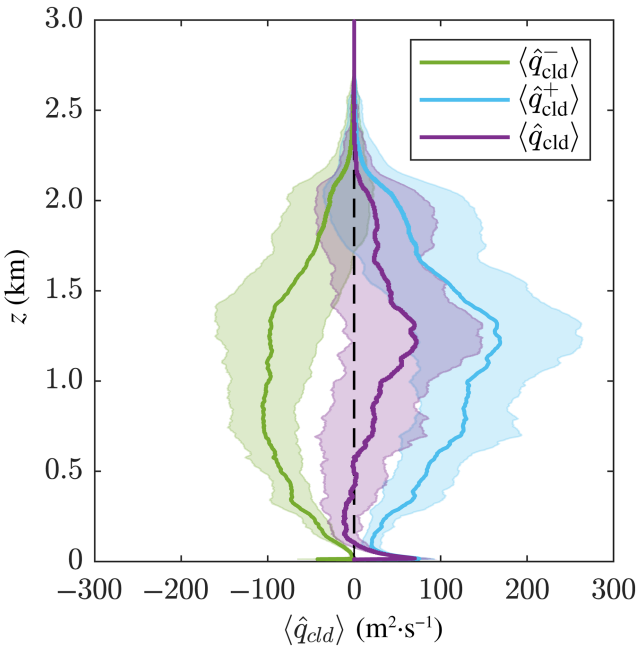

FIGURE 9 The time-averaged conditional net entrainment $\langle \hat{q}_{\rm cld} \rangle$ and its underlying components: $\langle \hat{q}^{-}_{\rm cld} \rangle$ from entrainment events, and $\langle \hat{q}^{+}_{\rm cld} \rangle$ from detrainment events. The coloured band shade represents one standard deviation around the time-average mean.

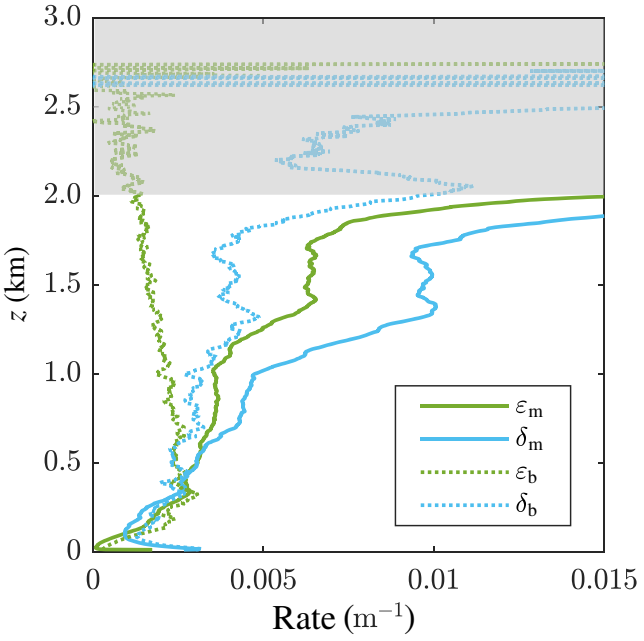

FIGURE 10 The vertical variation of the entrainment rates calculated using two different principles: solid lines mark the entrainment rate $\varepsilon_{\rm m}$ and detrainment rate $\delta_{\rm m}$ measured directly from the conditional data, and the dotted lines mark those estimated when evoking the bulk assumption, $\varepsilon_{\rm b}$ and $\delta_{\rm b}$. The data within the grey shade are statistically affected by relatively few, very small valued, observations of $\langle \hat{Q}_{\rm cld} \rangle$—this region is excluded in the analysis.

standard deviation from the time-averaged mean and indicate the relatively wide time variation in the entrainment and detrainment fluxes.

To parametrise the entrainment and detrainment, a dimensional (fractional) entrainment rate $\epsilon(z)$ and detrainment rate $\delta(z)$ are used, which represent the ratio of the entrainment and detrainment flux per unit height to the local vertical volume flux (Siebesma, 1998; Siebesma *et al.*, 2003):

$$\varepsilon_{\rm m} = \frac{|\langle \hat{q}^{-}_{\rm cld} \rangle|}{\langle \hat{Q}_{\rm cld} \rangle}, \quad \delta_{\rm m} = \frac{\langle \hat{q}^{+}_{\rm cld} \rangle}{\langle \hat{Q}_{\rm cld} \rangle}, \tag{30}$$

where the absolute value of the entrainment ensures the rates are defined positively. The dimension of entrainment and detrainment rate is m^{-1}, and the subscript "m" denotes the local entrainment and detrainment measurement at the boundary.

Previous LES studies could not explicitly measure the local entrainment $\langle \hat{q}^{-}_{\rm cld} \rangle$ and detrainment $\langle \hat{q}^{+}_{\rm cld} \rangle$. Instead, a bulk assumption (Betts, 1973) is used to determine an entrainment rate that relates vertical gradients in the cloud-averaged property $\langle \chi_{\rm cld} \rangle$ to the difference between these cloud values and the environment:

$$\frac{d\langle \chi_{\rm cld} \rangle}{dz} = -\varepsilon_{\rm b}(\langle \chi_{\rm cld} \rangle - \chi_{\rm e}), \tag{31}$$

where the scalar χ can be either the $\theta_{\rm l}$ or $q_{\rm t}$, and $\chi_{\rm e}$ is herein taken to be the background environmental value. The detrainment rate $\delta_{\rm b}$ is then determined together with the volume (mass) conservation equation as

$$\frac{d\langle \hat{Q}_{\rm cld} \rangle}{dz} = -(\varepsilon_{\rm b} - \delta_{\rm b})\langle \hat{Q}_{\rm cld} \rangle. \tag{32}$$

Note that the subscript "b" denotes the rates obtained using the bulk assumption, and this assumption is only valid when the cloud fraction (the ratio of the cloud area to the total simulation area) is close to zero (de Roode *et al.*, 2000), which is satisfied in the present simulation since the average cloud area fraction is generally less than 0.5% (see Figure 6a).

With the conditionally averaged data, Figure 10 presents the entrainment and detrainment rates measured directly from our data, Equation (30), and the estimates that would be inferred by evoking the bulk assumption, Equations 31 and 32. As the rates are not likely dependent on the choice of χ (Betts, 1973; Siebesma *et al.*, 2003), we take $\chi = q_{\rm t}$. Note that the rates above $z \approx 2,000$ m (shown in a grey shade) are affected by very small values of $\langle \hat{Q}_{\rm cld} \rangle$ and should be disregarded.

The estimates inferred by evoking the bulk assumption show that the detrainment rate generally increases with height, but the entrainment rate generally decreases; the magnitude of these rates is typically in the range of 0.002–0.006 m^{-1} and broadly similar to one another for heights $z \lesssim 700$ m. These results are generally consistent with Siebesma *et al.* (2003), which shows that, under the bulk assumption, our conditional data on an individual cloud give similar entrainment and detrainment rates to those from LES data of cloud ensembles.

However, the direct measurements of these rates from our data show that both the entrainment rate and detrainment rate grow with height. Most crucially to weather prediction and climate models, our data show that direct measurements of entrainment and detrainment rates are about a factor of 2 larger than estimation inferred using the bulk assumption; this finding is also consistent with the other direct measurements within the literature (Romps, 2010). Note that both evaluation methods provide detrainment rates that exceed the entrainment rates above around $z \approx 700$ m, which is consistent with the evolution of the net entrainment. The bulk assumption underestimates these rates, largely because it overestimates the concentration of the scalar within the fluid that is detrained from the cloud; this is the case since the detraining fluid comes from within regions close to the cloud edge, where the concentration of the scalar tends to be lower than the characteristic scale within the cloud (de Rooy *et al.*, 2013; Romps, 2010).

4.5 | Linking entrainment to cloud dynamics

Figure 5d presented the time series of the instantaneous net entrainment $\hat{q}_{cld}$ over the height of the cloud (where the blue region represents net entrainment, and red represents net detrainment). Entrainment data were collected from $t = 2,700$ s onwards. The figure clearly showed that above $z \approx 1,000$ m the cloud growing stage is associated with large net entrainment and the cloud dissipation stage with large net detrainment from the cloud. Net entrainment and detrainment above 1,000 m are strongly correlated to the in-cloud, horizontally averaged, buoyancy b_{cld} (Figure 5c). Indeed, in the growth stages of pulses, the buoyancy b_{cld} is positive and corresponds to negative $\hat{q}_{cld}$ (i.e., net entrainment); in the dissipation stage, the buoyancy b_{cld} is negative and corresponds to positive $\hat{q}_{cld}$ (i.e., net detrainment). Figure 5d also showed the net detrainment (red region) takes a longer time than the net entrainment (blue region) above 1,000 m, which suggests that the cloud has a time-averaged net detrainment, consistent with Figure 9.

In order to investigate the influence of buoyancy on entrainment, we perform a further conditioning of our directly measured entrainment and detrainment fluxes on the instantaneous, horizontally averaged, cloud buoyancy. The vertical variation in the time-averaged net entrainment/detrainment, conditioned on when average cloud buoyancy at that height is positive (i.e., $b_{cld}(z,t) > 0$), is shown by the purple line in Figure 11a; the purple line in Figure 11b shows net entrainment/detrainment data conditioned on when average cloud buoyancy is locally negative (i.e., $b_{cld}(z,t) < 0$). Interestingly, the data show that, above $z \approx 1,000$ m, at times when the horizontally averaged buoyancy is locally positive the cloud is net entraining; conversely, when the horizontally averaged buoyancy is locally negative the cloud is net detraining. Further investigation on the individual entrainment and detrainment components (green and blue lines respectively in Figure 11a,b) shows that the time-averaged entrainment does not vary significantly in the two buoyancy states, whereas the time-averaged detrainment is lower when $b_{cld}(z,t) > 0$ and is apparently greater when $b_{cld}(z,t) < 0$ over $z \approx 1,000$ m. This difference is the primary reason for the net entrainment in $b_{cld}(z,t) > 0$ but net detrainment in $b_{cld}(z,t) < 0$.

Figure 11c–f presents quadrant plots of the instantaneous cloud data capable of indicating correlations between the instantaneous entrainment fluxes $\hat{q}_{cld}(z,t)$ and instantaneous local buoyancy $b_{cld}(z,t)$ at four different heights: $z = \{1,000, 1,400, 1,800, 2,200\}$ m. Note that there are less data for higher elevations (e.g., $z = 2,200$ m) due to the intermittent presence of the cloud at greater heights being lessened. Data falling in the bottom half of these quadrant plots corresponds to the statistics shown in Figure 11b; that is, data of $b_{cld}(z,t) < 0$. These quadrant plots show that at instants when the cloud is locally negatively buoyant (at these heights) the net detrainment is typical (i.e., $\hat{q}_{cld} > 0$). In contrast, examination of the data falling in the top half of these quadrant plots shows that at instants when the cloud is locally positively buoyant (at these heights) the net entrainment is typical (i.e., $\hat{q}_{cld} < 0$)—this is especially the case at the higher heights; that is, $z = 1,800$ and 2,200 m. These data distributions support observations of the time-averaged net entrainment in $b_{cld} > 0$ and net detrainment $b_{cld} < 0$ shown in Figure 11a,b.

Note that at all heights the bottom right quadrant ($\hat{q}_{cld} > 0$ and $b_{cld} < 0$), which represents the instantaneous net detrainment by locally negatively buoyant cloud regions, has the most data samples and occurred most frequently. The data samples in this quadrant also tend to exhibit much larger amplitude than data in the other three

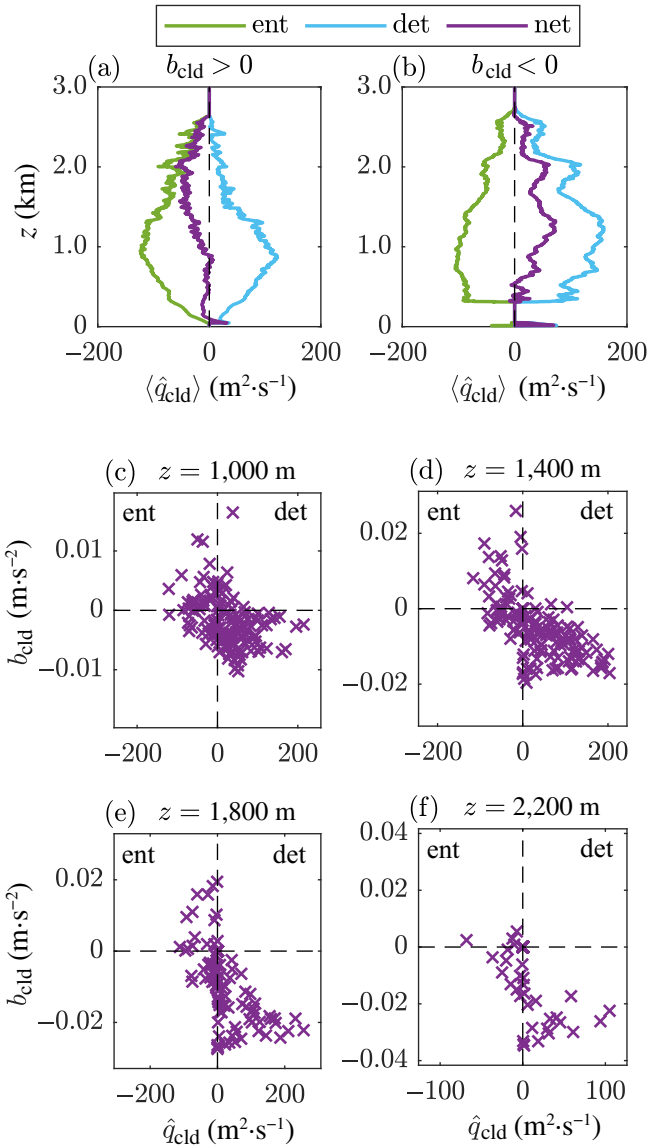

FIGURE 11 (a,b) Vertical variation in the time-averaged entrainment, detrainment, and net entrainment conditioned based on the in-cloud buoyancy, at the given height and instant is (a) positive $b_{cld}(z, t) > 0$ and (b) negative $b_{cld}(z, t) < 0$. (c–f) Quadrant plots showing the distribution of the local net entrainment $\hat{q}_{cld}(z, t)$ and local in-cloud buoyancy $b_{cld}(z, t)$ data pairs from four selected heights within the cloud.

quadrants. This directly results in greater time-averaged net detrainment (the purple line in Figure 11b). The reason for this greater net detrainment in the negatively buoyant period can be explained as follows: the negative buoyancy indicates that evaporation has occurred, which itself leads to a shrinkage of the cloud area; therefore, the cloud boundary then excludes this fluid, which is observed as detrainment.

5 | CONCLUSION

A fully resolved simulation of a shallow cumulus cloud from a maintained source in a quiescent environment was performed to investigate the turbulent entrainment and detrainment processes relevant to these clouds. Under a constant environmental condition and a constant supply of moist warm air at the cloud base, the system produced puffs (or cyclic pulses) that moved upwards and then collapsed. These findings are consistent with Heus *et al.* (2009), who argued that puffs are intrinsic to the cloud dynamics by exploring the link between the horizontal divergence of air and the rise of puffs.

The set-up deployed, which provided statistically stationary sub-cloud layer dynamics, allowed analysis of these quasi-steady cloud flow statistics for the first time. These were examined using two perspectives: (1) Reynolds-averaged statistics and (2) conditionally averaged statistics, both at the updraught and cloud boundaries. In both approaches, the cloud boundary was defined by the loci of points at which the liquid water specific humidity decreased to a very small threshold, and the updraught boundary was defined by the loci of points where the vertical velocity was zero within the cloud. The

cloud downdraught region was defined by the volume between these two boundaries.

The Reynolds-averaged and conditionally averaged statistics provide two distinctive perspectives on entrainment. The Reynolds-averaged viewpoint provides global information about the cloud behaviour averaged over several cycles. The conditionally-averaged statistics provide local information about the net transport across the instantaneous interfaces.

The Reynolds-averaged statistics show that environmental fluid near the cloud top at about 2 km height is entrained into the cloud, which is then mixed into the downdraught region and is detrained from the cloud at the neutral buoyancy level at about 1 km height. The updraught predominantly detrains with a maximum around the neutral buoyancy level (1 km).

The conditionally averaged statistics show that the cloud edge detrains over most of the height, presumably because of the evaporation that takes place at the cloud edge. For the updraught region, there is net entrainment into the updraught below 1 km and net detrainment above this level. The conditionally averaged statistics are generally consistent with the findings from the conditional statistics of LES studies of these clouds (e.g., Siebesma *et al.*, 2003). We observed that the net entrainment is strongly correlated with the rising puffs, consistent with Heus *et al.* (2009).

The conditional-statistics framework described in this article enabled independent calculation of the entrainment and detrainment fluxes (see Huang *et al.*, 2023b) over the height at the cloud boundary. The results show that entrainment and detrainment fluxes are large compared with the net entrainment flux. At heights for which detrainment tends to be relatively large or small, entrainment tends to be relatively large or small—both entrainment and detrainment peak at about the cloud half-height. Consistent with the direct measurements of Romps (2010), the subsequent entrainment and detrainment rates from our direct measurement are compared with the rates from the bulk assumption (de Rooy *et al.*, 2013; Siebesma *et al.*, 2003), which shows that the bulk approximation generally underestimates the entrainment and detrainment rates by nearly a factor of 2. Furthermore, we observed that the cloud net entrainment is strongly correlated with the cloud buoyancy, and this is confirmed by the segregated entrainment and detrainment metrics. These findings indicate that the cloud is likely to net entrain when the cloud's buoyancy is positive and is likely to net detrain when the cloud's buoyancy is negative.

Although the simulation performed here has a very high resolution, the Reynolds number ($Re = 30,000$) is much lower than that in reality, which is usually about 10^6–10^8 (Pruppacher & Klett, 2010; Siebesma & Cuijpers, 1996), and one could wonder what the effect is of the Reynolds numbers. This is a challenging question, since there have been relatively few studies that investigate Reynolds number effects for resolved numerical simulations of this complexity. For free boundary-layer flows like jets, plumes, and fountains, Reynolds number effects are typically negligible beyond a certain threshold value of the source Reynolds number Re_s—generally 1,000 for plumes and fountains (Burridge *et al.*, 2015; Plourde *et al.*, 2008; Williamson *et al.*, 2008). The source Reynolds number of the flow here is $Re_s = 2,000$, which is above this threshold. However, these flows do not have internal phase changes, and therefore the cumulus case will not only depend on source conditions. Siems and Bretherton (1992) studied Reynolds number effects on a stratocumulus deck and concluded that the cloud-top mixing is not dependent on the Reynolds number beyond 2,500. They revealed that (1) a larger Reynolds number decreases the eddy diffusion, and (2) a larger Reynolds number significantly increases the small-scale motion, which increases the cloud–environment interface, which therefore compensates for the reduction in the eddy diffusion. The latter is a well-known feature of high Reynolds number free boundary layers (Brizzolara *et al.*, 2023; Sreenivasan, 1991; Van Reeuwijk & Holzner, 2014). However, we note that the stratocumulus case is distinct from a cumulus case, in that there is no strong inversion layer present in the current simulation. Further investigation, including for example whether the Reynolds number affects the partition of entrainment–detrainment between updraught and cloud, would be an interesting avenue for future work.

ACKNOWLEDGEMENTS

We acknowledge the UK Turbulence Consortium (EPSRC grant EP/R029326/1) for the grand challenge project that provided the computational resources for this work. We thank the reviewers for their insightful feedback, which greatly contributed to the refinement of this work.

CONFLICT OF INTEREST STATEMENT

The authors report no conflict of interest.

DATA AVAILABILITY STATEMENT

The data that support the findings of this study are openly available in Zenodo at https://doi.org/10.5281/zenodo.14548736

ORCID

Jingzi Huang https://orcid.org/0000-0003-1668-1034
Henry C. Burridge https://orcid.org/0000-0002-0719-355X

Stephan R. de Roode https://orcid.org/0000-0003-3217-8009
Maarten van Reeuwijk https://orcid.org/0000-0003-4840-5050

REFERENCES

Abma, D., Heus, T. & Mellado, J.P. (2013) Direct numerical simulation of evaporative cooling at the lateral boundary of shallow cumulus clouds. *Journal of the Atmospheric Sciences*, 70(7), 2088–2102.

Ansong, J.K., Kyba, P.J. & Sutherland, B.R. (2008) Fountains impinging on a density interface. *Journal of Fluid Mechanics*, 595, 115–139. Available from: https://doi.org/10.1017/S0022112007009093

Arabas S, Axelsen S, Attema J, Azizi V, Beets C, Boeing SJ, et al. 2023. Dalesteam/dales: Dales 4.4.1.

Arakawa, A. & Schubert, W.H. (1974) Interaction of a cumulus cloud ensemble with the large-scale environment, part i. *Journal of the Atmospheric Sciences.*, 31(3), 674–701.

Betts, A.K. (1973) Non-precipitating cumulus convection and its parameterization. *Quarterly Journal of the Royal Meteorological Society*, 99(419), 178–196.

Bloomfield, L.J. & Kerr, R.C. (2000) A theoretical model of a turbulent fountain. *Journal of Fluid Mechanics*, 424, 197–216.

Bony, S., Stevens, B., Frierson, D., Jakob, C., Kageyama, M., Pincus, R. et al. (2015) Clouds, circulation and climate sensitivity. *Nature Geoscience*, 8, 261–268. Available from: https://doi.org/10.1038/ngeo2398

Bretherton, C.S. (2015) Insights into low-latitude cloud feedbacks from high-resolution models. *Philosophical Transactions of the Royal Society A: Mathematical, Physical and Engineering Sciences*, 373(2054), 20140415. Available from: https://doi.org/10.1098/rsta.2014.0415

Brizzolara, S., Mollicone, J.P., van Reeuwijk, M. & Holzner, M. (2023) Entrainment at multi-scales in shear-dominated and Rayleigh–Taylor turbulence. *European Journal of Mechanics - B/Fluids*, 101, 294–302.

Burridge, H.C., Mistry, A. & Hunt, G. (2015) The effect of source Reynolds number on the rise height of a fountain. *Physics of Fluids*, 27(4), 047101.

Corrsin, S. (1956) Some current problems in turbulent shear flows. Chapter 15, Proc. 1st Symposium on Naval Hydro., *National Academy of Sciences-National Research Council, 1957*, Washington, D.C., (515), 24–28.

Craske, J. & Van Reeuwijk, M. (2015) Energy dispersion in turbulent jets. Part 1. Direct simulation of steady and unsteady jets. *Journal of Fluid Mechanics*, 763, 500–537.

Da Silva, C.B., Hunt, J.C., Eames, I. & Westerweel, J. (2014) Interfacial layers between regions of different turbulence intensity. *Annual Review of Fluid Mechanics*, 46(1), 567–590.

Dawe, J.T. & Austin, P.H. (2011) The influence of the cloud shell on tracer budget measurements of les cloud entrainment. *Journal of the Atmospheric Sciences*, 68(12), 2909–2920. Available from: https://doi.org/10.1175/2011JAS3658.1

de Roode, S.R. (2007) Thermodynamics of cumulus clouds. *Física de la Tierra, 2007*, 19, 175–188.

de Roode, S.R., Duynkerke, P.G. & Siebesma, A.P. (2000) Analogies between mass-flux and reynolds-averaged equations. *Journal of the Atmospheric Sciences*, 57(10), 1585–1598.

de Roode, S.R., Siebesma, A.P., Jonker, H.J.J. & de Voogd, Y. (2012) Parameterization of the vertical velocity equation for shallow cumulus clouds. *Monthly Weather Review*, 140(8), 2424–2436. Available from: https://doi.org/10.1175/MWR-D-11-00277.1

de Rooy, W.C., Bechtold, P., Fröhlich, K., Hohenegger, C., Jonker, H., Mironov, D. et al. (2013) Entrainment and detrainment in cumulus convection: an overview. *Quarterly Journal of the Royal Meteorological Society*, 139(670), 1–19.

Elvidge, A.D. & Renfrew, I.A. (2016) The causes of foehn warming in the lee of mountains. *Bulletin of the American Meteorological Society*, 97(3), 455–466. Available from: https://doi.org/10.1175/BAMS-D-14-00194.1

Everson, R. & Sreenivasan, K. (1992) Accumulation rates of spiral-like structures in fluid flows. *Proceedings of the Royal Society A: Mathematical, Physical and Engineering Sciences*, 437(1900), 391–401.

Fernando, H.J.S. (1991) Turbulent mixing in stratified fluids. *Annual Review of Fluid Mechanics*, 23(1), 455–493.

French, J.R., Vali, G. & Kelly, R.D. (1999) Evolution of small cumulus clouds in Florida: observations of pulsating growth. *Atmospheric Research*, 52(1), 143–165. Available from: https://doi.org/10.1016/S0169-8095(99)00024-1

Grabowski, W.W. & Morrison, H. (2021) Supersaturation, buoyancy, and deep convection dynamics. *Atmospheric Chemistry and Physics*, 21(18), 13 997–14 018. Available from: https://doi.org/10.5194/acp-21-13997-2021

Heus, T. & Jonker, H.J.J. (2008) Subsiding shells around shallow cumulus clouds. *Journal of the Atmospheric Sciences*, 65(3), 1003–1018.

Heus, T., Jonker, H.J.J., Van den Akker, H.E.A., Griffith, E.J., Koutek, M. & Post, F.H. (2009) A statistical approach to the life cycle analysis of cumulus clouds selected in a virtual reality environment. *Journal of Geophysical Research: Atmospheres*, 114, D06208.

Heus, T., van Heerwaarden, C.C., Jonker, H.J.J., Pier Siebesma, A., Axelsen, S., van den Dries, K. et al. (2010) Formulation of the Dutch Atmospheric Large-Eddy Simulation (DALES) and overview of its applications. *Geoscientific Model Development*, 3(2), 415–444. Available from: https://doi.org/10.5194/gmd-3-415-2010

Holland, J.Z. & Rasmusson, E.M. (1973) Measurements of the atmospheric mass, energy, and momentum budgets over a 500-Kilometer Square of Tropical Ocean. *Monthly Weather Review*, 101(1), 44–55.

Huang, J., Burridge, H.C. & van Reeuwijk, M. (2023a) The internal structure of forced fountains. *Journal of Fluid Mechanics*, 961, A31. Available from: https://doi.org/10.1017/jfm.2023.210

Huang, J., Burridge, H.C. & van Reeuwijk, M. (2023b) Local entrainment across a TNTI and a TTI in a turbulent forced fountain. *Journal of Fluid Mechanics*, 977, A13. Available from: https://doi.org/10.1017/jfm.2023.947

Jonker, H.J.J., Heus, T. & Sullivan, P.P. (2008) A refined view of vertical mass transport by cumulus convection. *Geophysical Research Letters*, 35(7), L07810. Available from: https://doi.org/10.1029/2007GL032606

Katzwinkel, J., Siebert, H., Heus, T. & Shaw, R.A. (2014) Measurements of turbulent mixing and subsiding shells in trade wind cumuli. *Journal of the Atmospheric Sciences*, 71(8), 2810–2822. Available from: https://doi.org/10.1175/JAS-D-13-0222.1

Lenderink, G., Siebesma, A.P., Cheinet, S., Irons, S., Jones, C.G., Marquet, P. et al. (2004) The diurnal cycle of shallow cumulus

clouds over land: a single-column model intercomparison study. *Quarterly Journal of the Royal Meteorological Society*, 130(604), 3339–3364. Available from: https://doi.org/10.1256/qj.03.122

Mellado, J.P. (2017) Cloud-top entrainment in stratocumulus clouds. *Annual Review of Fluid Mechanics*, 49(1), 145–169.

Morrison, H., Peters, J.M., Varble, A.C., Hannah, W.M. & Giangrande, S.E. (2020) Thermal chains and entrainment in cumulus updrafts. Part I: theoretical description. *Journal of the Atmospheric Sciences*, 77(11), 3637–3660. Available from: https://doi.org/10.1175/JAS-D-19-0243.1

Morton, B.R., Taylor, G.I. & Turner, J.S. (1956) Turbulent gravitational convection from maintained and instantaneous sources. *Proceedings of the Royal Society of London*, 234(1196), 1–23.

Nair, V., Heus, T. & van Reeuwijk, M. (2021) A lagrangian study of interfaces at the edges of cumulus clouds. *Journal of the Atmospheric Sciences*, 78(8), 2397–2412.

Peters, J.M., Morrison, H., Varble, A.C., Hannah, W.M. & Giangrande, S.E. (2020) Thermal chains and entrainment in cumulus updrafts. Part ii: analysis of idealized simulations. *Journal of the Atmospheric Sciences*, 77(11), 3661–3681. Available from: https://doi.org/10.1175/JAS-D-19-0244.1

Plourde, F., Mv, P., Kim, S.D. & Balachandar, S. (2008) Direct numerical simulations of a rapidly expanding thermal plume: structure and entrainment interaction. *Journal of Fluid Mechanics*, 604, 99–123. Available from: https://doi.org/10.1017/S0022112008001006

Pruppacher, H. & Klett, J. (2010) *Microphysics of clouds and precipitation*. Dordrecht: Springer.

Rauber, R.M., Stevens, B., Ochs, H.T., Knight, C., Albrecht, B.A., Blyth, A.M. et al. (2007) Rain in shallow cumulus over the ocean: the rico campaign. *Bulletin of the American Meteorological Society*, 88(12), 1912–1928.

Romps, D.M. (2010) A direct measure of entrainment. *Journal of the Atmospheric Sciences*, 67(6), 1908–1927.

Siebert, H. & Shaw, R.A. (2017) Supersaturation fluctuations during the early stage of cumulus formation. *Journal of the Atmospheric Sciences*, 74(4), 975–988. Available from: https://doi.org/10.1175/JAS-D-16-0115.1

Siebesma, A.P. (1998) *Shallow cumulus convection*. Netherlands: Dordrecht: Springer, pp. 441–486. Available from: https://doi.org/10.1007/978-94-011-5058-3_19

Siebesma, A.P., Bretherton, C.S., Brown, A., Chlond, A., Cuxart, J., Duynkerke, P.G. et al. (2003) A large Eddy simulation Intercomparison study of shallow cumulus convection. *Journal of the Atmospheric Sciences*, 60(10), 1201–1219.

Siebesma, A.P. & Cuijpers, J.W.M. (1996) Evaluation of parametric assumptions for shallow cumulus convection. *Journal of the Atmospheric Sciences*, 52(6), 650–666.

Siems, S.T. & Bretherton, C.S. (1992) A numerical investigation of cloud-top entrainment instability and related experiments. *Quarterly Journal of the Royal Meteorological Society*, 118(507), 787–818. Available from: https://doi.org/10.1002/qj.49711850702

Sommeria, G. & Deardorff, J.W. (1977) Subgrid-scale condensation in models of nonprecipitating clouds. *Journal of the Atmospheric Sciences*, 34(2), 344–355.

Squires, P. & Turner, J.S. (1962) An entraining jet model for cumulo-nimbus updraughts. *Tellus*, 14(4), 422–434.

Sreenivasan, K.R. (1991) Fractals and multifractals in fluid turbulence. *Annual Review of Fluid Mechanics*, 23(Volume 23, 1991), 539–604. Available from: https://doi.org/10.1146/annurev.fl.23.010191.002543

Stephens, G.L. & Kummerow, C.D. (2007) The remote sensing of clouds and precipitation from space: a review. *Journal of the Atmospheric Sciences*, 64(11), 3742–3765. Available from: https://doi.org/10.1175/2006JAS2375.1

Townsend, A. (1976) *The structure of turbulent shear flow*. Cambridge, UK: Cambridge University Press.

Turner, J.S. (1986) Turbulent entrainment: the development of the entrainment assumption, and its application to geophysical flows. *Journal of Fluid Mechanics*, 173, 431–471. Available from: https://doi.org/10.1017/S0022112086001222

Van Reeuwijk, M. & Holzner, M. (2014) The turbulence boundary of a temporal jet. *Journal of Fluid Mechanics*, 739, 254–275. Available from: https://doi.org/10.1017/jfm.2013.613

Van Reeuwijk, M., Sallizoni, P., Hunt, G. & Craske, J. (2016) Turbulent transport and entrainment in jets and plumes: a DNS study. *Physical Review Fluids*, 1, 074301. Available from: https://doi.org/10.1103/PhysRevFluids.1.074301

Van Reeuwijk, M., Vassilicos, J.C. & Craske, J. (2021) Unified description of turbulent entrainment. *Journal of Fluid Mechanics*, 908, A12. Available from: https://doi.org/10.1017/jfm.2020.836

Wang, S., Wang, Q. & Feingold, G. (2003) Turbulence, condensation, and liquid water transport in numerically simulated nonprecipitating stratocumulus clouds. *Journal of the Atmospheric Sciences*, 60(2), 262–278. Available from: https://doi.org/10.1175/1520-0469(2003)060<0262:TCALWT>2.0.CO;2

Whiteman, C.D. (2000) *Mountain meteorology: fundamentals and applications*. New York: Oxford University Press.

Williamson, N., Srinarayana, N., Armfield, S.W., Mcbain, G.D. & Lin, W. (2008) Low-reynolds-number fountain behaviour. *Journal of Fluid Mechanics*, 608, 297–317. Available from: https://doi.org/10.1017/S0022112008002310

Wyngaard, J.C. (2010) *Turbulence in the atmosphere*. Cambridge, UK: Cambridge University Press.

Yurtoglu, M., Carton, M. & Storti, D. (2018) Treat all integrals as volume integrals: a unified, parallel, grid-based method for evaluation of volume, surface, and path integrals on implicitly defined domains. *Journal of Computing and Information Science in Engineering*, 18(2), 021013. Available from: https://doi.org/10.1175/JAS3414.1

Zhao, M. & Austin, P.H. (2005) Life cycle of numerically simulated shallow cumulus clouds. Part I: transport. *Journal of the Atmospheric Sciences*, 62(5), 1269–1290. Available from: https://doi.org/10.1175/JAS3414.1

SUPPORTING INFORMATION

Additional supporting information can be found online in the Supporting Information section at the end of this article.

How to cite this article: Huang, J., Burridge, H.C., de Roode, S.R. & van Reeuwijk, M. (2025) Entrainment and detrainment statistics of a stationary shallow cumulus cloud. *Quarterly Journal of the Royal Meteorological Society*, 151:e4920. Available from: https://doi.org/10.1002/qj.4920